U.PORTO
FC FACULDADE DE CIÊNCIAS
UNIVERSIDADE DO PORTO

U.PORTO

U.PORTO
FC FACULDADE DE CIÊNCIAS
UNIVERSIDADE DO PORTO

Computational study of ion selective separation through graphene nanowindows

Carlos Manuel Silva Pereira

Dissertação de Mestrado apresentada à
Faculdade de Ciências da Universidade do Porto em
Química

2019

FC

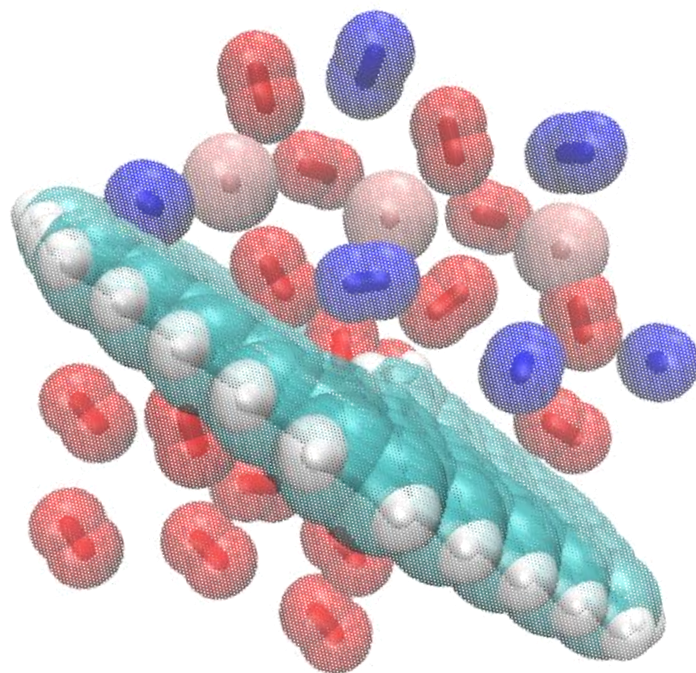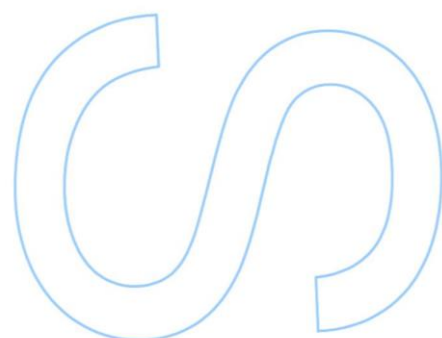# Computational study of ion selective separation through graphene nanowindows
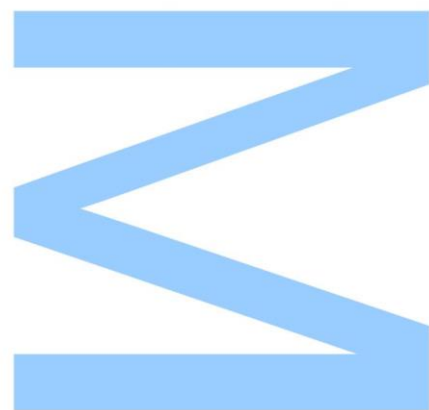
Carlos Manuel Silva Pereira

Mestrado em Química
DQB - Departamento em Química e Bioquímica
2019

Orientador
Alexandre L. Magalhães, UCIBIO/REQUIMTE,
FCUP - Faculdade de Ciências da Universidade do Porto

U.PORTO

FC **FACULDADE DE CIÊNCIAS**
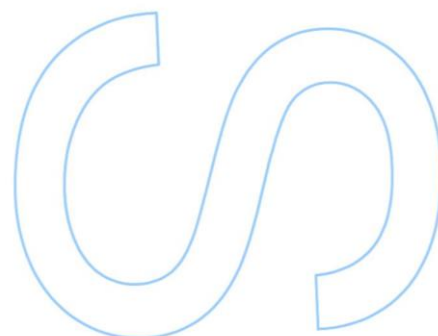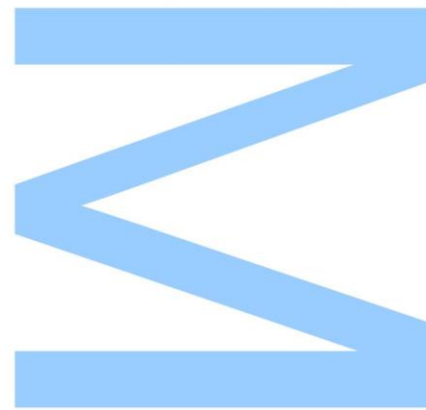UNIVERSIDADE DO PORTO

Todas as correções determinadas
pelo júri, e só essas, foram efetuadas.

O Presidente do Júri,

Porto, _____/_____/_____

This thesis was performed in the UCIBIO-REQUIMTE group at the Faculty of Sciences of the University of Porto, under the supervision of Professor Alexandre Lopes de Magalhães in the scholar year of 2018-2019. Coincidently enough, the current year has been proclaimed as the International Year of the Periodic Table of the Chemical Elements, IYPT 2019, in celebration of 150th anniversary of the discovery, by Dmitry Mendeleev, of one of the most important and influential feature in science. The development of the Periodic Table of the Elements provided several information that helped develop not only chemistry, but also physics, biology and other basic sciences. In order to honour this historic occasion, hereby I present one of the most outstanding quotes of Mendeleev.

' I saw in a dream a table where all the elements fell into place as required. Upon awakening, I immediately wrote it down on a piece of paper, only in one place did a correction later seem necessary.'

Dmitry Mendeleev

Agradecimentos

Com a entrega deste trabalho, a minha formação académica encontra-se perto duma das mais importantes fases da minha vida académica, que apesar de um pouco agitada e mais longa que o habitual, devido à aventura na Licenciatura de Matemática, permitiu moldar a minha pessoa e o meu futuro, pelo que agradeço a todos os intervenientes que ajudaram à conclusão desta etapa.

Em primeiro lugar, gostaria de agradecer ao meu orientador, o Professor Doutor Alexandre Lopes de Magalhães, pela oportunidade de desenvolver este trabalho consigo, e pelo apoio profissional e pessoal ao longo destes últimos meses. Agradeço imenso pelo seu apoio, motivação, ensinamentos e disponibilidade que demonstrou durante todo o período do projeto.

Agradeço à Professora Doutora Maria João Ramos, pela oportunidade de integração neste grupo de investigação de elevada excelência.

Ao Professor Doutor Eduardo Marques, pelos esclarecimentos nos assuntos relativos à entrega da tese, assim como de outras dúvidas que foram surgindo no decorrer do ano letivo.

Agradeço a todos os elementos do grupo UCIBIO, pela forma acolhedora com que fui recebido, e pela excelente atmosfera criada para o desenrolar do trabalho. Gostaria de dar um especial agradecimento ao Rui e ao João, e pela ajuda com as diversas dúvidas que foram surgindo; ao Óscar pelo apoio informático sempre que necessário e pelos momentos de descontração; e ao meu colega de trabalho, o Alexandre, pelo esclarecimento mútuo de dúvidas, que nos permitiu uma vasta aprendizagem continua e recíproca.

Gostaria também de agradecer à Professora Paula pela oportunidade de ensinar e de trabalhar no centro de estudos *Certific'arte*. O trabalho desenvolvido ao longos dos dois últimos anos permitiu uma estabilidade a nível financeira para que fosse possível a conclusão deste ciclo de estudos.

Aos meus colegas, Pedro e Margarida, um muito obrigado por toda a amizade e apoio durante estes anos.

Ao meu irmão, pelo apoio, amizade e admiração.

A ti, Catarina, agradeço-te imenso por todos os momentos em que estiveste ao meu lado, mesmo a vários quilómetros de distância. Obrigado por todo o apoio, carinho, compreensão e muita paciência que demonstraste ao longo deste ano. Ajudaste imenso nos momentos difíceis, e sem o teu apoio esta tese teria sido muito mais complicada.

Aos meus pais, um muito obrigado! Agradeço por todo o esforço que me proporcionou esta oportunidade de alcançar e de seguir os meus sonhos. Obrigado por, mesmo nestes meses complicados, nunca terem deixado de me apoiar e de me incentivar a acabar esta etapa. Agradeço-vos imenso por todo o amor e carinho, e por isso, dedico-vos esta tese.

Resumo

O grafeno é um nanomaterial derivado da grafite constituído por uma só camada de átomos de carbono com propriedades químicas e físicas excecionais, tendo sido utilizado em inúmeras aplicações. Uma das potenciais aplicações é o seu uso como membrana, devido à sua alta resistência mecânica, estabilidade química e possibilidade de se poder criar buracos neste material. Estes buracos, ou *'nanowindows'*, permitem ao grafeno ser uma alternativa sustentável aos processos tradicionais de separação que recorrem a transições de fase, uma vez que permitem uma permeação seletiva, rápida e com baixo consumo energético. A utilização de membranas permite assim uma alternativa aos processos convencionais, visto que com a utilização destas é possível obter dispositivos que requerem um menor consumo de energia, complexidade mecânica e equipamentos associados. Estas membranas de grafeno podem também ser utilizadas como alternativas para a dessalinização da água do mar.

A permeação dos principais constituintes do ar foi estudada para diferentes membranas nanoporosas, e a caracterização computacional destas foi realizada com recurso ao funcional M06-2X e a base de funções 6-31G(d). Com o presente trabalho, é possível uma comparação entre cálculos quânticos (QM) e estudos de dinâmica molecular (MD) que se encontram na literatura. Nestes são tomadas em consideração algumas aproximações que não permitem a descrição correta da natureza da membrana e da *nanowindow*, visto que estas são flexíveis.

Tendo em conta os resultados obtidos, é possível a reprodutibilidade dos nossos estudos, aplicando em diferentes membranas a metodologia descrita, tanto em vácuo como em solução. Os resultados aqui demonstrados, em conjunto com os da literatura, permitem sugerir que estas membranas nanoporosas podem tornar-se alternativas para futuras membranas de separação de ar.

Keywords: grafeno nanoporoso, nanowindows, teoria funcional da densidade, química quântica, estudos de permeação, barreiras energéticas

Abstract

Graphene is a single-atom carbon material that has been used as a membrane due to their chemical and physical properties such as high mechanical strength, chemical stability and ability to be converted into a sieve. Therefore, graphene containing nanowindows could be used as selective, fast and energy-efficient membrane for separation processes. These membranes provide a sustainable alternative to the traditional phase transitions separation processes, since these devices are characterized by low energy consumption, reduced mechanical complexity and small equipment; and can also be used as an alternative membrane towards the desalination of sea water if proven to be efficient.

The main constituents of air were demonstrated to permeate through these different pores and the computational characterization of these nanowindows were performed using the functional M06-2X and the basis set 6-31G(d). With the present work, it is possible a comparison between quantum calculations (QM) and studies performed in the literature mostly using molecular dynamics (MD). In the latter, there are some approximations that are performed that do not allow for the correct description of the flexible membrane and their nanowindow-rim chemistry.

Futhermore, it was also performed the parametrization of our studies, in order to apply this methodology towards different membranes in both vacuum and solution. The results demonstrated here, in conjunction with those present in the literature suggest that these nanowindows could become alternatives for future air separation membranes.

Table of contents

Index of Figures

Index of Equations

Index of Tables

List of Abbreviations

AFM	Atomic Force Microscopy
B3	Three-parameter Becke functional
B3LYP	Becke 3 and Lee, Yang and Parr Functional
B88	Becke1988 functional
B95	Becke 1995 functional
CASU	Cryogenic air separation unit
CNTs	Carbon nanotubes
DFT	Density functional theory
fallout	Freeze all atoms outside the nanowindow
foutnoh	Freeze all atoms outside the nanowindow, except the graphene edges
GGA	Generalized gradient approximation
GTO	Gaussian type orbital
HF	Hartree-Fock
HOMO	Highest occupied molecular orbital
IYPT	International year of the periodic table
KCIS	Krieger, Chen, Iafrate and Savin functional
KS	Kohn-Sham
LDA	Local density approximation
LSDA	Local spin-density approximation
LUMO	Lowest unoccupied molecular orbital
LYP	Lee, Yang and Parr functional
M06	Minnesota 06 functional
M06-2X	Minnesota 06-2X functional
MD	Molecular Dynamics
MM	Molecular mechanics

MWCNTs	Multi-walled carbon nanotubes
nof	No freeze
P	Perdew 1986 functional
PBE	Perdew-Burke-Ernzerhof functional
PCM	Polarizable continuum model
PES	Potential energy surface
PW91	Perdew 1991
QM	Quantum Mechanics
RMSD	Root-mean-square deviation
SCF	Self-consistent field
SLDB	Same level, different basis (QM/QM)
STP	Standard temperature and pressure
STO	Slater type orbital
SWCNTs	Single-walled carbon nanotubes
TMS	Thermal undulation spectra
TPSS	Tao, Perdew, Staroverov and Scuseria functional
VdW	van der Waals
VSXC	van Voorhis and Scuseria functional

A. BACKGROUND AND MOTIVATIONS

"*We're running the most dangerous experiment in history right now, which is to see how much carbon dioxide the atmosphere can handle before there is an environmental catastrophe*".

Elon Musk

The air separation industry uses conventional technologies that require a gas-to-liquid phase change in the mixture, in order to separate their components, which adds a significant energy cost to the separation cost [1]. Among several procedures, the cryogenic distillation of air (usage of CASUs - cryogenic air separation units) [2] and amine absorption of carbon dioxide (CO_2) from natural gases [3] have been the most explored in this industry. According to a study performed in 2016 [4], chemical separations process accounted for half of the total US industrial energy consumption (**Figure 1**). Moreover, the separations based on distillation process comprise for almost 8 % of the total US energy consumption, confirming the high carbon footprint due to carbon dioxide (CO_2) production [4, 5]. Thus, developing alternatives that don't require the usage of heat can drastically change the path to a sustainable future.
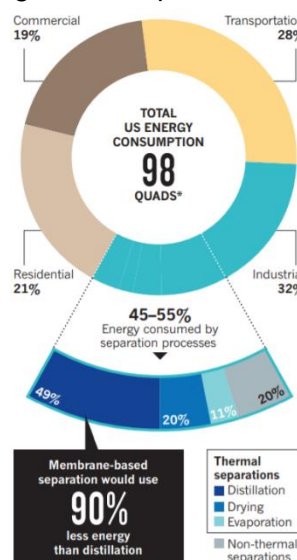
Figure 1 – US energy consumption distribution in 2016, adapted from [4].

Furthermore, the development and/or improvement of a separation process for the purification of water is essential. Even though the main compound in the surface of Earth is water, the scarcity of fresh water (drinkable) will become a necessity in the near future, due to the constant world population growth and greater energy demands [6]. In order to overcome this challenge, the creation of an appropriate desalination process of the sea water is required [7].

Efficient membrane technologies have the potential to shape the future, mastering the separations processes with high permeability, selectivity, processability and stability. Such desirable properties can be achieved using smaller equipment footprint, reduced

mechanical complexity, and less energy than traditional processes [5]. Thus, membrane separations result in low cost and eco-friendly processes, becoming more economical and environmentally attractive [1].

In this work, we developed a theoretical study on the permeability of graphene membranes towards the separation of several compounds in air. Our main goal is to, firstly, reproduce and characterize a highly porous carbon material reported in previous work with DFT calculations and then its application in permeation studies using the functional M06-2X and the basis set 6-31G(d). Finally, it was intended to study the interactions of permeating molecules through the graphene membrane.

This work is divided in the following chapters:

Chapter B - **Introduction**

A brief description of the main carbon nanomaterials and their properties is presented. In this chapter, the selection of the better carbon structure to use is discussed.

Chapter C - **Theoretical Background**

A short review of the quantum mechanics methodologies used during this project is described.

Chapter D - **Results and Discussion**

The obtained results will be presented in this chapter. Firstly, the characterization of the membranes in study is performed. In the following section, permeation through those membranes are studied and some insights about these studies are presented. The last section is related with the permeation study of these membranes in solution.

Chapter E - **Conclusions**

This final chapter will present the major conclusions of this work, and the advances that this work could contribute in the future.

Chapter F - **References**

All the bibliographic references used along this work are sorted in the order they appeared.

B. INTRODUCTION

"Nobody ever figures out what life is all about, and it doesn't matter. Explore the world. Nearly everything is really interesting if you go into it deeply enough".

Richard P. Feynman

1. Carbon

The existence of carbon in our universe dates back to fusion processes that occurred in older stars. The three-alpha process transforms three alpha particles (helium - ^4He) in a carbon nucleus (^{12}C), and occurs in red giants that have consumed most of their core hydrogen [8]. Carbon as an element is a key piece for most life in Earth as it acts as a main component of numerous different compounds, such as carbohydrates, proteins, and nucleotides, that were the essential for the origin of life as we know [9].

The ability to form the carbon-based compounds can be explained by the lowest state energy of this element. An isolated carbon has an electron configuration of $1s^2\,2s^2\,2p^2$ for its ground-state, characterized by four different valence electrons to bond and form new molecules. The orbitals in the $2p$ sublevel are degenerated in the three different orbitals, $2px$, $2py$ and $2pz$. The energy difference between the $2s$ and the $2p$ energy levels is very small (close to 4 eV), which allows that an electron can easily be excited to the empty $2p$ orbital. Upon electron excitation, the four different orbitals occupied have degeneracy and can mix together in a phenomenon called hybridization. The 2s atomic orbital interacts with n $2p$ orbitals, forming $n+1$ degenerated sp^n hybridized orbitals (n ranges from 1 to 3) (**Figure 2**) [10-12].
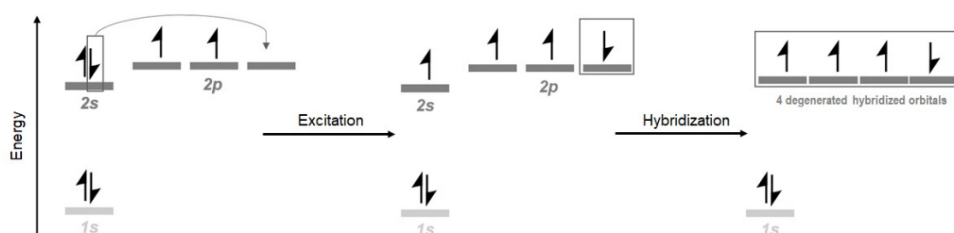
Figure 2 – Hybridization phenomenon in Carbon atoms.

The hybridized orbitals are used by carbon atoms to form σ bonds, while the remainder 2p unhybridized orbitals form π bonds. Therefore *sp* orbitals are responsible for the number of bonds that the carbon atom can establish and for the geometry of the generated molecule; and the 2*p* orbitals for the determination of the order of the covalent bond that is established [12]. The sp^3 hybridized carbon is responsible for the connection of four different atoms with single bonds in a tetrahedral arrangement with bond angles of *ca.* 109.5 º; the sp^2 connects with three atoms and forms a double bond with the 2*p* free orbital in a trigonal planar design with bond angles of *ca.* 120 º. Finally, the *sp* connects with two atoms in a linear geometry and, due to the two remaining 2*p* orbitals, can form two double bonds or one triple and one single, with bond angles close to 180 º.

The hybridization phenomenon is responsible for nearly 10 million carbon compounds with different types of structures. Even in elemental carbon this occurs naturally in three different allotropes: anthracite (coal), graphite and diamond. The latter two, show very different spatial arrangement due to the difference in the hybridization observed in each case, which makes the allotropes have different properties. The carbon phase diagram (**Figure 3**) is a good tool that can be used to demonstrate these differences [13].
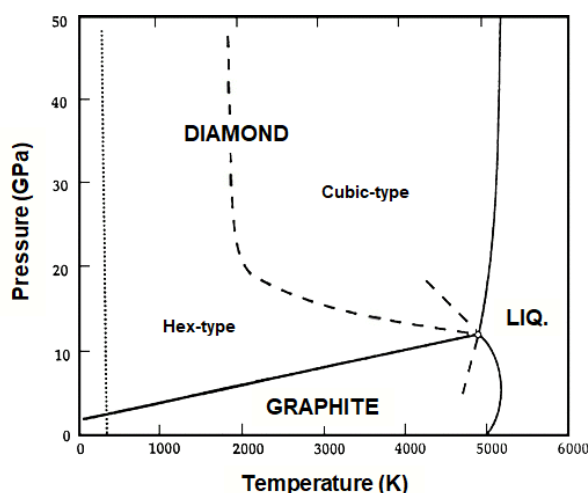
Figure 3 – Carbon phase diagram, adapted from [13].

From **Figure 3**, it is possible to see, that graphite is the more stable phase under STP conditions and, on the other hand, diamond is more stable at higher pressure and temperature. Graphite consists in a stable hexagonal layered structure, in which the carbon atoms are sp^2 hybridized and are connected with an average bond length of 1.42 Å, achieving a honeycomb lattice arrangement. The 2*p* leftover orbital is used to create π bonds between the carbon atoms that results in a π delocalized system for this structure. This property allows graphite to have high electrical conductivity [14].

In the diamond framework, carbon atoms are sp^3 hybridized and form a hard solid consisted by covalent bonds in a tetrahedron arrangement, that can achieve a cubic or hexagonal crystal structure, as it is observed in **Figure 3** [10, 15]. Diamond is used, not only as a gemstone, but also can be used in several technologic applications due to its properties, such as hardness, strength, high thermal conductivity and high chemical stability [16].

Recent developments have been using carbon nanomaterials as the key for next-generation technological devices. This emerging field started since the discovery of fullerenes in 1985 by Kroto *et al.* [17] (**Figure 4a**), followed by the carbon nanotubes in 1991 by Iijima [18] (**Figure 4b**), and last but not least, graphene in 2004 by Novoselov *et al.* [19] (**Figure 4c**). These nanostructured forms of carbon are being applied in several new applications owing to excellent properties.

a)

b)

c)
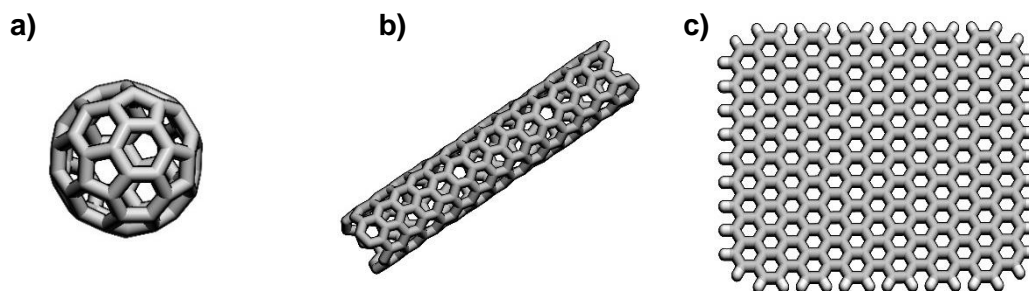
Figure 4 – Examples of carbon nanomaterials, a) Buckminster fullerene, b) carbon nanotube and c) graphene.

2. Fullerenes

Fullerenes (**Figure 4a**), also known as buckyballs, are closed hollow cages of carbon atoms, discovered by Harold W. Kroto, Robert F. Curl and Richard E. Smalley, during a work focused in explaining anomalous infrared and ultraviolet carbon spectra from outer space [17]. During these experiments, a structure containing 60 carbon atoms was discovered and due to its resemblances to the Architect Buckminster Fuller's 1960s geodesic domes, C_{60} was named buckminsterfullerene [10, 20]. Due to this discovery of a soccer ball-like structure, a new branch in carbon chemistry has been developed and it netted these two scientists the Nobel prize award in 1996 for "their discovery of fullerenes" [17, 21].

Since the development of fullerenes research, the creation of new simple and inexpensive production methods of these materials [20, 22, 23], gave rise to a world of opportunities for this material in several applications, such as the development of new drugs [24] and products [20].

2.1. Structural characterization

Fullerene discovery also marked the study of new allotropes of carbon. Until that moment, the structurally different forms of this element were diamond and graphite, as discussed before. Compared with the 3D diamond crystal lattice and the 2D graphite hexagonal lattice, fullerenes are considered has a 0D-carbon cluster that follows the Euler polyhedron characteristic, χ (**Equation 1**). According to this equation, a polyhedron composed of n vertices must always contain 12 pentagons in order to be able to close the ring structure [25, 26].

a) $$\chi = n - E + F$$

b) $$F = \frac{n}{2} + 2$$

c) $$H_F = \frac{n}{2} - 10$$

Equation 1 – Euler polyhedron characteristic, a) Euler formula, where n is the number of vertices; b) number of faces and c) number of hexagonal faces in a C_n fullerene.

The most studied fullerene is the buckminsterfullerene, C_{60} (**Figure 5a**), is an example of the application of this rule, in which the closed carbon cluster follows the structure of an truncated icosahedron, *i.e.*, a polygon with 60 vertices and 32 faces,

where 12 faces are pentagons and the remainder 20 are hexagons [27]. The C_{70} (**Figure 5b**) is another direct example of the application of this rule, in which we have a polygon with 70 vertices and 37 faces, where it is possible to observe 25 hexagonal faces and the 12 required pentagons [28].
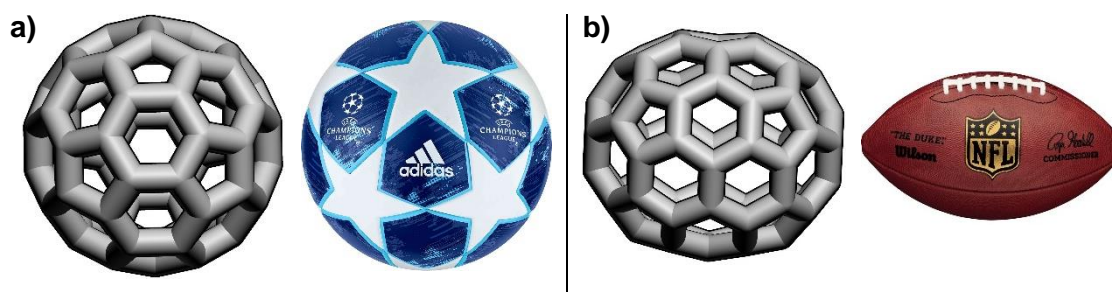
Figure 5 – Representation of the structure of a) C_{60}, buckminsterfullerene and b) C_{70}, with a comparison of the structure with a real-life object.

In fullerene structure each carbon is bonded to three other carbon atoms in a sp^2 hybridized network of carbon atoms, one electron of the $2s$ orbital is promoted to the $2p$ free orbital of carbon and then the orbitals are blended into three sp^2 hybridized orbitals, which are used for σ-bonding. A direct consequence of this is the formation of π-bonds from the remainder electron in the leftover $2p$ orbital. However, due to the curvature observed in this structure, there is a rehybridization between sp^2 and sp^3 [27, 29]. With that being said, the remainder π electron of each carbon atom is localized in the hexagonal rings which leads to a smaller bond length due to their increased double bond character. In C_{60}, there are two different types of bonds, the bonds that lie in the hexagonal rings (30) and the remainder form the edges that connect the pentagons with the hexagons (60). The bonds localized in the hexagonal rings have normally 1.38 Å length, and the ones that are used to connect the pentagons with the hexagons are a bit longer, *i.e.*, 1.45 Å [27, 29, 30].

C_{60} is the smallest fullerene and the most stable fullerene, followed by C_{70}, due to them being the firsts that obey the Euler's rule, *i.e.*, they have the 12 pentagons required to close the ring [26]. For fullerenes where isolated pentagons are impossible to exist, the more stable isomers are those with the smallest number of adjacent pentagons in their structure [31, 32].

The electronic structure of a fullerene can be used as a useful indicator of its stability, due to the observation of the gap between the highest occupied molecular orbital (HOMO) and the lowest unoccupied molecular orbital (LUMO) energy levels. A large difference between these orbitals equals a high kinetic stability on these type of

molecules [28]. Using once more, C_{60} as an example, the 60 free *p* orbitals that are responsible for the π-bonds will form 30 bonding molecular orbitals and 30 antibonding molecular orbitals, according with the Huckel π-molecular orbital diagram of C_{60}. From the direct analysis of this diagram, reported by Haddon R.C. *et al.* [29], the 60 electrons are occupying the 30 bonding orbitals that confirms the stability of the structure. The calculated band gap is similar to stable aromatic molecules, such as anthracene and tetracene [29]. The three low-lying degenerate LUMOs make this fullerene an electrophile because it can readily accept six additional electrons, that allows it to be a good semiconductor [10, 17].

2.2. Properties of Fullerenes

The fullerene molecular group has an interesting curvilinear shape that enables it to have great properties. They are very hard molecules, a single C_{60} molecule has a surprisingly high bulk modulus (668 GPa), that is even harder than steel (160 GPa) and diamond (442 GPa) and when compressed can bounce back to their original shape when the pressure is removed [33]. C_{60} has even been proved to have remarkable impact strength, as it is able to withstand high-speed collisions of up to 15,000 mph against stainless steel plate [10]. Even though fullerene is a kinetically stable structure owing to its geodesic and electronic properties, the release of this strain excess is responsible of the reactivity of this molecule [27]. Furthermore, the free three low-lying LUMOs are also triggered for the nucleophilic power [10].

These ball-like structures can be doped with metal atoms to achieve different electrical and thermal conductivity properties [34]; can be functionalized with polar species in order to convert their hydrophobic surfaces into hydrophilic surfaces, which can enhance diagnostic and therapeutic applications [27, 35]; and can encapsulate atoms inside its carbon cage to transport or enhance different properties [36, 37]. Taking into consideration their small size fullerenes are not able to be used as a membrane, however they can be induce ion permeability of lipid bilayer membranes via the formation of ion pores or conductive defects in their structure [38, 39].

3. Carbon nanotubes

Carbon nanotubes, CNTs (**Figure 3b**), are tubular-like structures made of carbon atoms and were described in the literature in 1952 [40] and 1976 [41], however it was only after the work performed by Iijima in 1991 [18] that these carbon nanomaterials started to be noticed in the scientific community. In Iijima work, it was synthetized *nanocarbons made of hollow tubes*, later named multi-walled carbon nanotubes (MWCNTs) (**Figure 5b**), using an electric arc-discharge evaporation method that was inspired in a fullerene synthesis procedure [18]. The jump towards a world-wide research area of interest happen after the first production of *single-atomic-layer walls*, also known as single-walled carbon nanotubes (SWCNTs) (**Figure 5a**), in 1993 by two different authors simultaneously [42, 43]. Currently, carbon nanotubes have already been reported in literature in a wide range of applications, from the development of new electronics [44, 45] to new opportunities in biotechnological research [46].

CNT materials follow shares some structural features with fullerenes, as they are capped at either end by half-a-fullerene and they contain sp^2-hybridized carbon atoms bonded to three other carbon atoms are arranged in a hexagonal-like pattern [10]. Carbon nanotubes also exhibit some differences in the π-bonding system due to the curvature observed.

As referred above, there are different types of carbon nanotubes, characterized by the number of layers of concentric tubes in the material. SWCNTs (**Figure 6a**) and MWCNTs (**Figure 6b**) are formed by one tube or more than one, respectively.
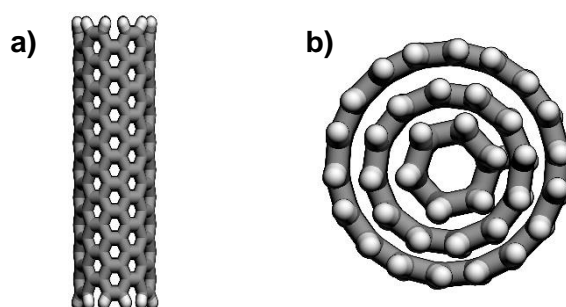
Figure 6 – Representation of the structure of a) SWCNTs and b) MWCNTs.

3.1. Structural characterization

The structure of a SWCNT can be described as a single sheet of graphite, known as graphene, that is rolled up into a tube-like shape, in the direction of a chiral vector (**Figure 7**). This vector goes from one carbon atom to an equivalent in the graphene

lattice, and it is defined by a linear combination of the real space basis vectors, that follow the chiral indices (m,n), as it is shown in **Equation 2** [47, 48].
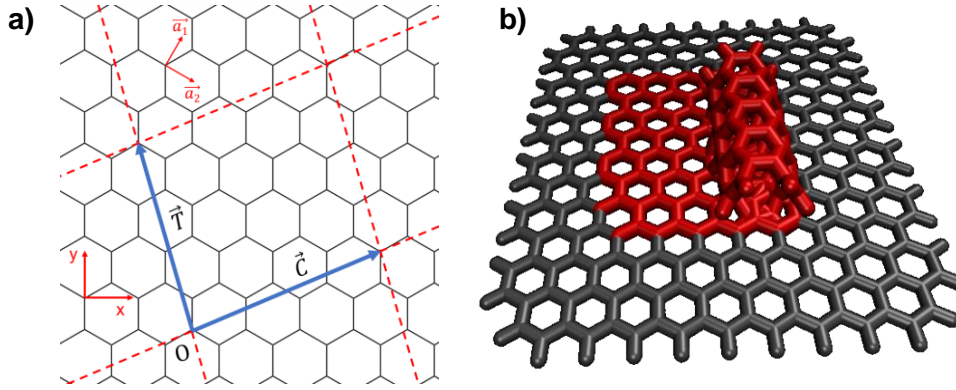
Figure 7 – Representation of a) the unit cell for carbon nanotubes, in which $\vec{C}$ is the chiral vector; and b) demonstration of the roll-up (defines tube axis) that occurs in when SWCNTs are formed.

$$\vec{C} = n \cdot \vec{a}_1 + m \cdot \vec{a}_2$$

Equation 2 – Chiral vector definition using the chiral indices (m,n), in which $\vec{a}_1$ and $\vec{a}_2$ are the lattice vectors of graphene.

Carbon nanotubes depend greatly on these indices, because they define the structural conformation that the sidewall of these materials can assume. These chiral indices are responsible to define other structural properties, such as the diameter of the resulting nanotube that equals the vector length (**Equation 3**); the angle between the chiral vector $\vec{C}$ and the zigzag direction (**Equation 4**); the translation vector $\vec{T}$ (**Equation 5**); and the unit cell of CNTs that is defined by $\vec{C} \times \vec{T}$ [47, 48]. Furthermore, SWCNTs can assume different spatial arrangement with different combinations of these integers, *i.e.*, (0,n) are zigzag (**Figure 8a**); (m,m) are armchair (**Figure 8b**) and (m,n) are chiral nanotubes (**Figure 8c**).

$$d = \frac{|\vec{C}|}{\pi} = \frac{a_0 \cdot \sqrt{n^2 + n \cdot m + m^2}}{\pi}$$

Equation 3 – Diameter of the circumference of the resulting nanotube; in which a_0 is the lattice constant of the graphene honeycomb lattice, typically $a_0 = 2.46$ Å [49].

$$\theta = \arctan\left(\frac{\sqrt{3}m}{2n + m}\right)$$

Equation 4 – θ corresponds to the angle between the chiral vector $\vec{C}$ and the zigzag direction.

$$\vec{T} = \frac{(2m + n) \cdot \vec{a}_1 - (2n + m) \cdot \vec{a}_2}{gdc(2m + n, \ m + 2n)}$$

Equation 5 – Definition of the translation vector $\vec{T}$, that connects two equivalent carbon atoms along the SWCNs axis; in which gdc is the greatest common divisor function.
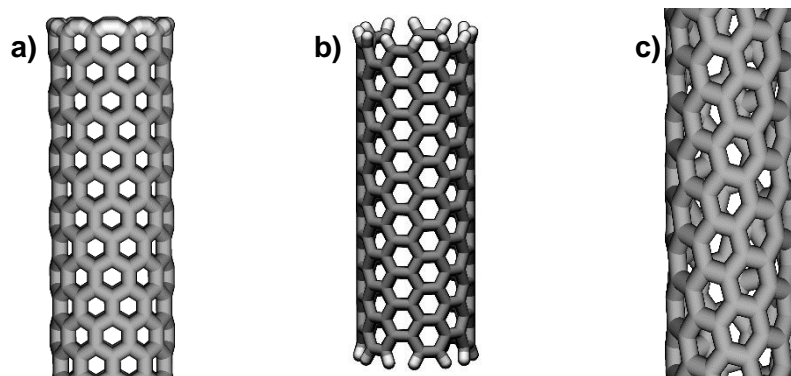
Figure 8 – Representation of a) zigzag (0,n), b) armchair (m,m) and c) chiral (m,n) SWCNTs.

With the direct observation of the latter figure, the hexagonal pattern in zigzag nanotubes is parallel to the tube axis, while the armchair pattern is oriented perpendicularly to the same axis. **Equation 4** defines the angle between the chiral vector and the zigzag direction, therefore the zigzag tubes exhibit an angle $\theta = 0$ º and the armchair tubes normally demonstrate $\theta = 30$ º. Chiral nanotubes comprise all the random patterns between the zigzag and armchair tubes. These tubes have a chiral angle of 0 °<θ<30 ° [47]. The zigzag and armchair tubes are more stable than the chiral due to these differences in symmetry.

The electronic properties of carbon nanotubes are usually derived from the properties of the graphene sheet (discussed in the following subchapter). The band structure for SWCNTs is obtained by the reciprocal lattice vectors, which are derived by the vectors that define the unit cell [50, 51]. The chiral vector is then used to define the band gap of the nanotubes, because as the rolling up of the graphite sheet occurs the electron wavefunctions are subjected to an additional quantization condition. Therefore, the electronic properties of SWCNTs depend greatly if these cut through the tip of the Dirac cones, leading to either a 1D metallic band structure (**Figure 9a**) or a semiconducting structure with a band gap (**Figure 9b**) [52]. The condition that allows the nanotube to be metallic is that $n = m$ or if $(n - m)$ is an integer multiple of 3. All the remaining 2/3 combinations, *i.e.* $(n - m) \neq$ 3i, make a semiconducting nanotube [48]. **Figure 9** illustrate in a simple approach, the carbon nanotube band structure.
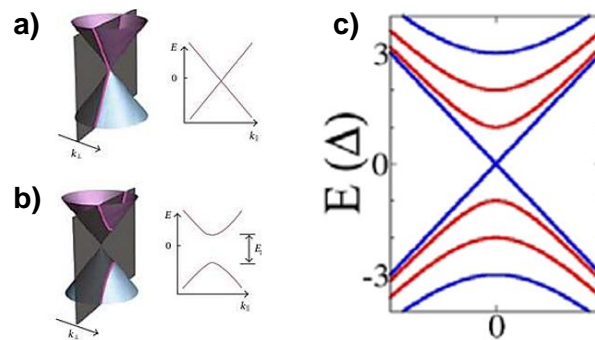
Figure 9 – Simplified model of an SWCNT band structure, (a) is a metallic SWCNT and (b) a semiconducting SWCNT, adapted from [53]; (c) representation of the overlap in bands present in a metallic nanotube (blue curves) and a semiconducting tube (red lines) with the same diameter d, adapted from [52].

In the latter schematic image, the black plane demonstrates how the additional quantization condition is introduced by the rolling up the graphene into the nanotubes. Essentially, a 1D crop is performed out of the formerly 2D band structure of graphene. In a) the plane intersects the tip of the cone, leading to a metallic SWCNT, and in b) the cut corresponds to semiconducting tube, as it does not intersect it [52, 53].

3.2. Properties of Carbon nanotubes

The properties of carbon nanotubes are derived from their structure and the strength of the C-C bond established through these tubular-shaped molecules. Similarly to fullerenes, these structures possess a very high Young's modulus (1.4 TPa) and tensile strength (100 GPa), which normally imply high mechanical resistance. However, they are an elastic material that is resilient to bend and can return back to their original form without any damage [10]. Carbon nanotubes have also high thermal conductivity, in their axial direction, that is equivalent to the thermal conductivity of the basal plane of graphite and natural diamond ($\lambda \approx 6600$ W·m^{-1}·K^{-1}) [54]. These structures, due to their tubular-like shape and near one-dimensional nature, allow charges to be carried through them with negligible resistance, resulting in the ability to sustain high current densities (up to 100 MA·cm^{-2}) [55] and having high carrier mobility (105 cm^{2}·V^{-1}·s^{-1}) [52]. These electronic properties allow carbon nanotubes to be used in electronic devices, such as computers [45]. With the functionalization of these structures it is also possible to achieve very different properties that can enhance several possible applications, such as the encapsulation and storage of hydrogen gas inside the nanotubes [56] and as a drug-delivery system [57].

CNTs can also be used as membranes, since they exhibit high flux, high permeability, low fouling and by functionalization in their tips offer a selective permeation

of molecules [58]. In order to be applied to separation processes, CNTs need to be always coupled in another structure, achieving this way, a well-ordered nanoporous membrane [59-61]. In these membranes, molecules can permeate through the inner cavity of this structure, as it was demonstrated in the literature for the water desalination processes using reverse osmosis [62-64] and for air separation processes [61, 65-67]. However, in order to carbon nanotube-based membranes be a possibility in the future, it is needed to be able to create a mechanism for the aligned-growth of CNTs and for the CNT-tip functionalization [58].

4. Graphene

Strangely enough, graphene was the last of the carbon nanomaterials to be isolated, even though it can be considered as the mother of all graphitic forms, since its structure can be a building material for buckyballs (0D), nanotubes (1D) and graphite (3D). The study around the *2D graphite* structure started seventy years ago [50], although its isolation was thought to be purely an academic and unstable material that wouldn't exist in its free state [68, 69]. The isolation of this material was performed by Andre Geim, Konstantin Novoselov and their group in 2004 [19], and since then, graphene has become one of the most promising and versatile materials ever discovered. In their work a process for the fabrication, identification and the characterization of this material was described using Atomic Force Microscopy (AFM) [19]. Graphene based materials have been attracting significant attention in several fields due to its properties, and several applications in different areas of study. The work that paved the way for this uprising nanomaterial by Geim and Novoselov ended up in a Nobel Prize award for both scientists in 2010 [70].

4.1. Structural characterization

Graphene is a two-dimensional one-atom-thick sheet of a *sp*^{2}-hibridized carbon system packed in a honeycomb crystal lattice, in which each carbon is strongly bonded to three other neighbouring carbon atoms in the layer by σ bonds with *ca.* 1.42 Å of length, similar to benzene.

The crystal structure of graphene can be made of two different geometrical constructions, as it is possible to see in **Figure 10**. The direct hexagonal lattice of graphene (**Figure 10a**) is defined by a rhombic unit cell (highlighted at grey) that is characterized by two vectors and two non-equivalent carbon atoms (A and B) that describe the two Bravais sublattices [47]. These basis vectors $(\vec{a}_1, \vec{a}_2)$ form between them an angle of π/3, have the same length and are defined as (**Equation 6**) [71]:

$$\vec{a}_1 = \left(\frac{\sqrt{3}a}{2}, \frac{a_0}{2}\right) \;\; ; \;\; \vec{a}_2 = \left(\frac{\sqrt{3}a}{2}, -\frac{a_0}{2}\right) \;\; ; \;\; |\vec{a}_1| = |\vec{a}_2| = a_0 = \sqrt{3}a_{c-c}$$

Equation 6 – Description of the basis vectors of the hexagonal lattice of graphene and demonstration of the length of these vectors ($a_{c-c} \approx 1.42$ Å normally).
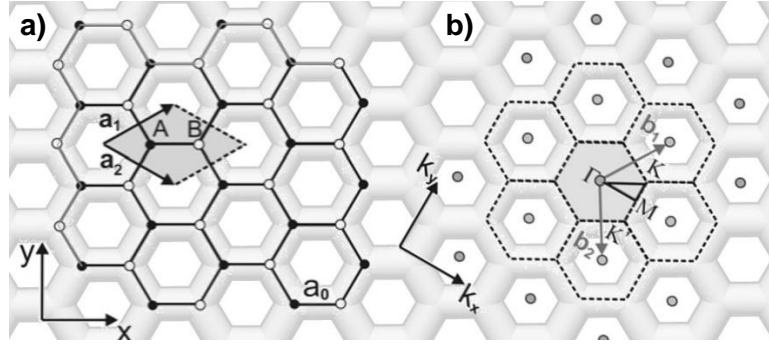
Figure 10 – Geometric structure of graphene, (a) direct lattice of graphene, defined by $(\vec{a}_1, \vec{a}_2)$, with the unit cell A_g highlighted at grey; and (b) reciprocal lattice, defined by (b_1, b_2), with the first Brillouin zone marked at grey, which contains the high symmetry points, Γ, K, K' and M are indicated, adapted from [47].

The reciprocal lattice of graphene (**Figure 10b**) is characterized by a unit cell that is defined by the two reciprocal lattice vectors $(\vec{b}_1, \vec{b}_2)$. These also have the same length but form an angle of 2π/3 and are described by (**Equation 7**) [71]:

$$\vec{b}_1 = \left(\frac{2\pi}{\sqrt{3}a_0}, \frac{2\pi}{a_0}\right) \; ; \; \vec{b}_2 = \left(\frac{2\pi}{\sqrt{3}a_0}, -\frac{2\pi}{a_0}\right) \; ; \; |\vec{b}_1| = |\vec{b}_2| = b_0 = 4\pi\sqrt{3}a_0$$

Equation 7 – Description of the basis vectors of the reciprocal lattice of graphene and demonstration of the length of these vectors.

The direct Bravais and reciprocal lattices, as well as, the unit cell areas from both lattices are related due to their relation in the definition of the components of their vectors and are defined as (**Equation 8**) [72]:

$$\vec{a}_i \cdot \vec{b}_j = 2\pi \cdot \vec{\delta}_{ij} \; ; \; A_g \cdot B_g = (2\pi)^2$$

Equation 8 – Relation between the direct and reciprocal lattice of graphene and their areas.

In Figure 9, the high symmetry points (Γ, K, K' and M) are also showed. They have an important role to depict the electronic properties of graphene because their low-energy excitations are centred around the two points K and K', also known as Dirac points [14] and can be defined as (**Equation 9**) [71]:

$$K = \left(\frac{2\pi}{\sqrt{3}a_0}, \frac{2\pi}{\sqrt{3}}\right) \; ; \; K' = \left(\frac{2\pi}{\sqrt{3}a_0}, -\frac{2\pi}{\sqrt{3}}\right)$$

Equation 9 – Definition of the Dirac points in graphene.

Before its isolation, graphene was thought as a purely academic material due to its possibly poor stability. This idea came from a research on 2D crystals that had been studied theoretically and demonstrated that thermal fluctuations resulted in the melting down of these 2D crystals at finite temperatures [68, 69]. This theory had even been supported by experimental work that showed that below a thin film thickness, films became unstable [47, 73]. Currently, it is known that graphene as a 2D material is stable

due to the in-plane and out-of-plane distortions of the graphene lattice, at the cost of the reduction of some electronic properties [68, 74-76].

Before its experimental isolation, the electronic band structure of graphene was already calculated by Wallace in 1947 [50]. Graphene contains four valence electrons for each carbon atom, in which three of them are used to form bonds in each lattice with strong connections. The resultant obtained framework is a stable hexagonal structure in which an electron can move freely between the positive ions of the lattice. Thus, the latter is responsible for the unique electronic and conduction properties.

In order to explain graphene electronic band structure, the reciprocal lattice is normally used, because the electronic bands are defined along specific reciprocal directions within the Brillouin zone. Taking into consideration that electrons can jump to both the nearest or to the next nearest neighbor in graphene, the tight-binding Hamiltonian is given by **Equation 10** [71]:

$$\hat{H} = -t \sum_{\langle i,j \rangle, \sigma} \left(a_{\sigma,i}^\dagger b_{\sigma,j} + H.c. \right) - t' \sum_{\langle\langle i,j \rangle\rangle, \sigma} \left(a_{\sigma,i}^\dagger a_{\sigma,j} + b_{\sigma,i}^\dagger b_{\sigma,j} + H.c. \right)$$

Equation 10 – Description of the tight-binding Hamiltonian, in which t (the carbon-carbon interaction is ≈2.8 eV) is the nearest neighbor hopping energy, t' is the next neighbor hopping energy and $a_{\sigma,j}$ ($a_{\sigma,i}^\dagger$) creates an electron with spin σ on the sublattice A (or B).

With this simple approach, it is possible to adequately describe graphene by considering a single π electron per atom, that leads to **Equation 11** [72]:

$$E^\pm(k_x, k_y) = \pm t \sqrt{1 + 4\cos\frac{\sqrt{3}k_x a_0}{2}\cos\frac{k_y a_0}{2} + 4\cos^2\frac{k_y a_0}{2}}$$

Equation 11 – Resultant function for the π electron dispersion relation in graphene.

Thus, the electronic band structure of graphene can be defined (**Figure 11**). The positive part of the resultant function (E^+) denotes the conduction band and the negative (E^-) corresponds to the valence band. These bands meet at the high symmetry points K and K', also named Dirac points. Carbon atoms in graphene are characterized by contributing one electron to the valence band, whilst leaving the conduction band empty, as such the Fermi level, is precisely at the energy where conduction and valence bands meet.
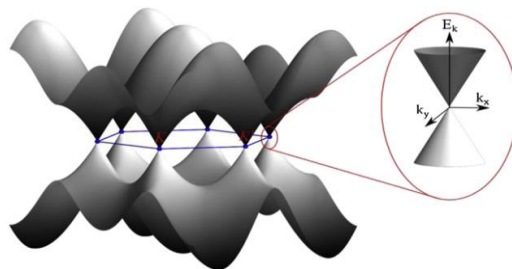
Figure 11 – Band structure of graphene, a) showing the conductance (upper band) and valence bands (lower band) meeting at the Dirac points (K, K') in blue; b) closeup of the Dirac cones, showing the point where the energy bands touch, adapted from [77].

The electronic band structure of graphene allows this material to be described as a zero-gap semiconductor. This is possible due to the Dirac point having no energy gap between the bands and this being the place at which the density of states (DOS) is zero [77]. Close to the Fermi energy level, the band structure of graphene can be described in terms of two inequivalent Dirac cones situated at the Dirac points, which leads to the charge carries having unique properties, that can be described by the relativistic Dirac equation, except that for graphene the Fermi velocity ($v_F \approx 0,87\text{x}10^6\,\text{m}\cdot\text{s}^{-1}$) of electrons or holes replaces the speed of light [10, 77]. These charge carriers are best described as massless Dirac fermions that move through the graphene lattice at high speeds (15000 $\text{cm}^2\cdot\text{V}^{-1}\cdot\text{s}^{-1}$) [10, 68].

4.2. Properties of graphene

The electronic and geometric structure of graphene allow it to have amazing properties for several applications. This carbon nanomaterial is one of the strong materials ever discovery, similarly to the other carbon nanomaterials (fullerenes and nanotubes). It possesses a very high Young's modulus (~1.1 TPa) and tensile strength (~130 GPa) [78], while remaining flexible and very light ($\rho = 0.77$ $\text{mg}\cdot\text{m}^{-2}$) [79]. This material is also able to stretch up to 20 % of its initial length [10], has a very high theoretical specific area (~ 2630 $\text{m}^2\cdot\text{g}^{-1}$) [79] and contains the ability to outperform carbon nanotubes in heat conduction due to its high value of thermal conductivity at room temperature ($5.30 \pm 0.48 \times 10^3$ $\text{W}\cdot\text{m}^{-1}\cdot\text{K}^{-1}$) [80]. As referred before, graphene has extraordinary electronic properties, such as the high charge carrier mobility, with values greater than 15000 $\text{cm}^2\cdot\text{V}^{-1}\cdot\text{s}^{-1}$ [68, 81]; its low resistivity (10^{-6} ohm·cm) [68]; and the high charge carrier density (2×10^{11} cm^{-2}) [81]. These are considered remarkable electronic properties for the application of this material in electronic devices, like touch screens, solar cells and sensors [10].

Summing it up, this single-atom-thick planar structure, is one of the most exciting materials that currently exist because it is at the same time the lightest and the strongest material in the world and has the ability to conduct heat and electricity better than anything else, which leads to becoming a good material for countless applications, such as bioelectric sensory devices [82], optical electronics [83], filtration processes [5, 84], photovoltaic cells [85] and energy storage [86].

All of the properties listed above, correspond to that of an idealized one-atom-thick graphene, thus it is important to note that these properties may vary a little bit when working with other types of graphene. Graphene can contain defects or be covalent functionalized, which leads to some different properties of this nanomaterial [10].

4.3. Usage as a membrane

Graphene has standout properties that can be applied in several fields. Due to their 2D dimensions, it was immediately thought has a potential membrane for filtration and separation processes. The atomic thickness, high mechanical strength, chemical stability and ability to be converted into a sieve allow this amazing nanomaterial to be used as a membrane [5]. With this in mind, researchers started to test the permeability of graphene, and it was rapidly proved, both experimentally and theoretically, that it was impermeable to even the smallest of gases, Helium [84, 87]. This occurs due to the electronic structure of graphene sheet, as the delocalized electron clouds of π-orbitals occupy the voids of the aromatic rings, preventing completely the permeation [88]. However, it was observed that it is possible for protons to permeate directly to the graphene layer [89, 90]. These properties allow graphene to be applied as a barrier for gases and liquids, or as a protector for metallic surfaces against corrosion [88].

In order to achieve permeation through this layer, it is necessary to create nanopores in graphene, through functionalization. Currently, in the literature there are several methods that are being develop for graphene fabrication with pores, making industrial-scale production of these membranes a future possibility, *e.g.*, ion bombardment [91], template-synthesized mesh [92], and high-temperature oxidation [93]. This new porous graphene is then able to permit negligible pore transport resistance and exhibit ultra-fast molecular permeation. Depending on the functionalization of the nanopore in graphene, it is possible to transport and separate different molecules, achieving even the ability to open and close, *i.e.*, the creation of nanowindows [5]. These graphene membranes have been studied to be applied in several areas, and have been proved to work exceptionally well in gas separation

processes [5, 94-102] and in water desalination [7, 103-107]. In these several studies, it is possible to see that by controlling the pore size and the different types of functionalization in the windows edges, it is possible to alter the permeation rate, as well as, the permeation through the membranes.

Most of these studies have been made using molecular dynamics (MD) simulations, therefore more specific quantum calculations are yet to be performed. The work we are going to describe in this reported is focused around fulfilling some of the voids of the literature, as most existing studies contains various cases of over-simplified cases that disregard the dynamic nature of these membranes. As in several of these computational studies of gas separation processes that were reported, the full permeation mechanism of the membranes is not studied due to the lack of protonation in the nanopore edge and too idealized symmetries [96, 99], as well as the lack of any heteroatom [96, 101, 102]; and the usage of a rigid membrane framework [97, 100, 101].

C. THEORETICAL BACKGROUND

"It is also a good rule not to put too much confidence in experimental results until they have been confirmed by theory".

Sir Arthur Eddington

Computational chemistry, often called theoretical chemistry, is nowadays a field of great importance to understand several new and complex systems, such as graphene and large biological systems. This area of study traces back to the early part of the twentieth century with the discovery of Max Planck black body radiation curve, that resulted in the early development of quantum mechanics (QM). Throughout the years, the technological advances on computers science and engineering enabled an exponential growth of this field at an outstanding rate. Currently, computer simulations achieve higher levels of accuracy without increasing significantly the computational cost.

Even though computational chemistry is renowned for its level of accuracy, the experimental data can also reveal important information about the complex structures in study. Thus, the combination between theory and experiment is relevant and it has been accelerating the progress of science in several areas of study.

A chemist that works in this theoretical area has the possibility to use three different quantum methods to fully describe the chemical system under study. Briefly, the quantum calculations are named ab initio, semi-empirical and density-functional theory, that differ in the computational cost required, the accuracy and the type of approximation method. Moreover, there is the possibility to describe the atomic interactions based on classic methods, using Molecular Mechanics (MM). This method is a powerful tool to describe the conformation space of a system; however, this approximation does not include electron description, which is a major drawback in the calculation chemical reactions. In the recent decades, there have been the development of hybrid methods, such as QM/QM or QM/MM, that divide the system in two different parts and describe them with different approximations.

The chemical properties of the system in this study was described using QM and QM/QM methodologies, and these are fully described with more detail in this chapter.

1. Quantum Mechanics

In the early years of the atomic and subatomic studies, classical physicists were not able to describe these systems, which leaded to the beginning of the development of the quantum theory. This theory traces back to the discovery of Max Planck black-body radiation in 1901, in which was described that the quantity of energy emitted by a true black-body only is dependent on its temperature (**Equation 12**) [108, 109].

$$E = \hbar \upsilon$$

Equation 12 – Planck's proportional relation between energy and the radiation frequency, in which υ is the frequency and $\hbar$ is the Max Plank's constant ($\hbar = 6.626069 \times 10^{-34}$ J·s).

This discovery by Planck allowed Einstein to fully describe the photoelectric effect in 1905 [110]. Einstein started to picture electromagnetic radiation as composed by particles. Bohr's atomic model of the hydrogen atom came afterwards in 1913 [111], with the help of Rutherford scattering experiments, in which he demonstrated that electrons are under a quantization condition as they occupy certain energetic levels, *i.e.*, orbitals. The atomic model allowed to comprehend that the electron movement is performed by jumping between the energy levels, *i.e.*, the emission and absorption of energy [108]. It was only in 1924 that the wave-particle duality was proposed by De Broglie [112], that demonstrated that electrons are waves with a particular wavelength and depend on the particle's momentum (**Equation 13**).

$$\lambda = \frac{h}{p}$$

Equation 13 – De Broglie wavelength.

The wave nature of particles was comproved experimentally in 1926 by Davisson and Germer [113]. In this experiment they fired a beam of electrons directly to a nickel crystal and observed the reflection of the electrons off the surface of the crystal to form an interference pattern (both constructive and destructive), which is a characteristic behavior of a typical for wave-like disturbances [114].

In 1927 Heisenberg introduced a formulation that indicated that in order to predict exactly the quantum position of a particle, the less precisely its momentum can be known (**Equation 14**) [115].

$$\sigma_x \sigma_p \geq \frac{\hbar}{2}$$

Equation 14 – Heisenberg's uncertainty principle, in which σ_x and σ_p are respectively the position and momentum errors and $\hbar$ is the reduced Planck's constant ($\hbar = h/2\pi$).

This observation imposes a limit of how much predictions can we have about the behavior of any physical system. The equation that fully describes how electrons, atoms and molecules have wave-like properties was created by Schrödinger. According with this equation, it is possible to know how a system evolves with time and it can be considered one of the fundamental postulates of Quantum Mechanics. This discovery in conjunction to the work performed by the other physicists mentioned before leaded to a new understanding of a quantum system. Thus, quantum mechanics can be defined with at least, five postulates. Firstly, the state of a quantum mechanical system can be defined mathematically [116]:

Postulate I

The state of a quantum mechanical system is completely specified

by a function $\Psi(r,t)$.

This postulate defines one physical system as a wave function Ψ that depends only on their spatial coordinates $r = (x, y, z)$ and time (t). Ψ represents the probability amplitude, *i.e.*, it gives the probability of finding a particle as a function of their position.

Secondly postulate is related to the information that is available to be obtained about the system [116]:

Postulate II

To every observable property in classical mechanics A, there corresponds a linear Hermitian operator $\hat{A}$, allowing a complete set of eigenfunctions.

The third postulate is related to the latter, as it describes that to each type of measurement of a Hermitian operator $\hat{A}$, results in the eigenvalues a of the operator (**Equation 15**) [116-118].

Postulate III

$$\hat{A}\,\Psi(r,t) = a\,\Psi(r,t)$$

Equation 15 – Third postulate of quantum mechanics, in which $\hat{A}$ is the operator for a certain system property; and a is the corresponding eigenvalue for that property.

The fourth postulate is related with the time-dependent Schrödinger equation (**Equation 16**), in which the operator is the Hamiltonian ($\hat{H}$), and the given eigenvalue is the total system energy (E) [116-118].

Postulate IV

$$\widehat{H}\Psi(r,t) = E\Psi(r,t) = i\hbar \cdot \frac{\partial \Psi}{\partial t}$$

Equation 16 – Time-dependant Schrödinger equation, in which i is the imaginary unit.

Finally, the fifth postulate is related with the Pauli exclusion principle, as two identical fermions can not have the same quantum state [117].

Postulate V

The wave function Ψ is antisymmetric for the exchange of coordinates between
identical fermions, as the probability density of the same position
with the same spin coordinate is equal to zero.

The definition of these five postulates described above is somewhat debatable as different authors nominate different postulates [116-118]. Nevertheless, the above are considered a good framework for quantum mechanics and will be an important tool to understand the following concepts.

1.1 The Hamiltonian

For the definition of the time-dependent Schrödinger equation, the Hamiltonian was introduced. This operator is associated with the total energy of an hydrogen-like system and it is also described as the sum of the kinetic ($\widehat{T}$) and the potential energy ($\widehat{V}$) operators (**Equation 17**) [116-119].

$$\widehat{H} = \widehat{T} + \widehat{V}$$

Equation 17 – Hamiltonian description.

The potential operator can be described as the potential energy of the elements in the system using a Coulombic-like potential, $V(r,t)$. The kinetic operator, $\widehat{T}$, is calculated based on the Laplacian operator (divergence of the gradient ∇, of the cartesian coordinates), both defined in **Equations 18**.

$$V(r,t) = -\frac{Ze^2}{4\pi\varepsilon_0 r} \; ; \; \widehat{T} = -\frac{\hbar^2}{2m_e} \cdot \left(\frac{\partial^2}{\partial x^2} + \frac{\partial^2}{\partial y^2} + \frac{\partial^2}{\partial z^2} \right)$$

Equation 18 – Definition of the Hamiltonian operators.

Thus, the Hamiltonian description in **Equation 17** can be written with more detail as the sum of the operators (**Equation 19**).

$$\hat{H} = \hat{T} + \hat{V} = -\frac{\hbar^2}{2m_e} \cdot \nabla^2 + V(r,t)$$

Equation 19 – Kinetic energy calculation.

Considering a Hamiltonian composed by M nuclei and N electrons. For this system it must be considered the different interactions between these species: the kinetic energy of the protons and the electrons, and the potential energy that characterizes the attraction between the nuclei and the electrons, as well as the repulsion between identical species. Thus, the Hamiltonian is characterized into five different terms (**Equation 20**), in which $\hat{T}_M$ and $\hat{T}_N$ are the kinetic operators for nuclei and electrons, and $\hat{V}_{MN}$, $\hat{V}_{NN}$ and $\hat{V}_{MM}$ are the potential operators for the interactions nuclei-electrons, electrons-electrons and nuclei-nuclei, respectively.

$$\hat{H} = \hat{T}_M + \hat{T}_N + \hat{V}_{MN} + \hat{V}_{NN} + \hat{V}_{MM}$$

Equation 20 – Hamiltonian description in a system composed by M nuclei and N electrons.

The fully expanded Hamiltonian is described in the next equation [117, 119]:

$$\hat{H} = -\frac{1}{2}\sum_{i=1}^{N}\nabla_i^2 - \frac{1}{2}\sum_{A=1}^{M}\frac{1}{M_A}\nabla_A^2 - \sum_{i}^{N}\sum_{A}^{M}\frac{Z_A}{r_{iA}} + \sum_{i-j}^{N}\frac{1}{r_{ij}} + \sum_{A-B}^{M}\frac{Z_A Z_B}{r_{AB}}$$

Equation 21 – Expanded Hamiltonian in a system composed by M nuclei and N electrons.

1.2 Schrödinger Equation

The solutions of the Schrödinger equation (**Equation 16**) is dependent on the Hamiltonian description. These possible solutions would allow the full description of atomic and subatomic systems; however solving it is not mathematically achievable for more than two interacting particles ($M \geq 2$) or polyelectronic systems [119]. Thus, it is possible to approximate this equation to a more feasible one that is independent on time and is a function of the space coordinates of the particles of the system (**Equation 22**) [116-119].

$$\hat{H}\Psi(r) = E\Psi(r)$$

Equation 22 – Time independent Schrödinger Equation.

The latter equation allows to determine indirectly the probability to find particles based in the position r, through the calculation of the wave function and energy. Even though this approach simplifies the resolution of the Schrödinger equation, it neglects relativistic effects and only represents the probability at a certain time. Thus, it is imperative to introduce other approximations such as the variational principle. This

method allows the use of an arbitrary wave function (Ψ_t) to obtain the lowest energy of the system, in order to get closer to the real fundamental state energy. It is proven mathematically that this approach always provides an equally to a greater value of the real one, E_0 (**Equation 23**).

$$\frac{\int \Psi_t^* \, \hat{H} \, \Psi_t \, d\tau}{\int \Psi_t^2 \, d\tau} \geq E_0$$

Equation 23 – Variational principle.

Another method that can be taken into consideration is the Born-Oppenheimer approximation. A proton is 1836 times heavier than an electron and, therefore it is possible to consider that protons move much slower than electrons, leading to the possibility of the electrons to rearrange around the nuclei instantly whenever there are nuclear motions. This approximation simplifies greatly the Hamiltonian for more complex systems as it allows to describe the wave function in two different parts: the electronic ($\hat{H}_{el}$) and the nuclear Hamiltonian ($\hat{H}_n$) (**Equation 24**) [116-119].

$$\hat{H} = \hat{H}_{el} + \hat{H}_n$$

Equation 24 – The Born-Oppenheimer approximation.

With the Born-Oppenheimer approximation the Hamiltonian of a system, composed by M nuclei and N electrons (**Equation 25**), is described by the electronic Hamiltonian that considers the nuclei to be fixed in space with zero kinetic energy and the nuclear-nuclear interactions constant; and the nuclear Hamiltonian is calculated by the sum of the kinetic energy of nuclear movements and the potential energy associated with the internuclear repulsion.

$$\hat{H}_{el} = \hat{T}_N + \hat{V}_{MN} + \hat{V}_{NN} \;\; ; \;\; \hat{H}_n = \hat{T}_M + \hat{V}_{MM}$$

Equation 25 – Electronic and nuclear Hamiltonian based on the Born-Oppenheimer approximation.

Mathematically, the Born-Oppenheimer approximation is not enough to enable the resolution of the Schrödinger equation when we consider a polyelectronic system. Thus, several theories and methodologies were developed in order to facilitate the interpretation and determination of the chemical and physical properties of a system.

After the Born-Oppenheimer approximation, researchers started to depict the information that the electronic and nuclear Hamiltonian could provide. The electronic Hamiltonian provides the biggest contribution to the overall system energy, due to the fixation of the nuclei position; thus some methodologies are centered in the accurate description of electrons in molecules, in order to perform the calculation of the electronic

energy of the system in a less expensive way. This approach also provides a lot of information about some chemical properties of the system, such as the potential energy surface (PES) and the respective equilibrium geometries.

The electronic Hamiltonian characterization is performed using different approximation methods and can be separated into two different categories, *i.e.*, those based on the wave function or on the electron density.

1.3 Wave function-based theories

The wave function-based theories utilize the wave function to achieve the resolution of the electronic Hamiltonian of the Schrödinger equation for a system capable of containing more particles. The methodologies applied can be divided in two different type of approaches: the *ab initio* and the semi-empirical.

Ab initio calculations describe an electron system through the introduction of a simplification to their description. In an independent-particle model, the motion of one electron is considered to be independent of all the remainder, which leads to either neglecting all interactions between the particles with the exception of the most important or by taking an average value of all the interactions [120]. *Ab initio* methods are accurate, although they require high computational effort and can only be performed for a few number of atoms. The most commonly used *ab initio* methods are those based on the Hartree-Fock theory (HF).

Using semi-empirical methods there is the possibility of simplifying even further these calculations, through the HF based formalism that employ several approximations based on the accurate substitution of certain parameters by experimentally obtained results. This allows a much larger system and leads to a lesser computational demand, however it is conditioned by existing experimental data of molecular analogues of the system in study. A briefly description of the HF theory, basis of both methodologies, can be found in the next section.

1.3.1 Hartree-Fock Theory

With the development of the HF theory, any system could be accurately characterized if there was no limit to the computational resources. This theory introduces an approximation that assumes the correlation between electrons is discarded. In other words, it is neglected the electronic repulsion between electrons while only accounting for the average electron-electron interactions [120].

In the HF theorem, each electron is considered to be moving in relation to an electrostatic field created by the nuclei and the average field of the other electrons. This describes each one-electron system wave function, $\phi_i(r_i)$, and the total wave function is given as a product of these orbitals, $\Psi_{Hartree}(r_i)$ (**Equation 26**) [120, 121].

$$\Psi_{Hartree}(r_i) = \prod_i^n \phi_i(r_i)$$

Equation 26 – Overall Hartree wave function as a product of each one-electron wave functions.

HF calculations always start with the employment of the variational principle, in order to generate a guess wave function close to the real one for each electron. After this, and following the Pauli exclusion principle, in which the total wave function must be antisymmetric with respect to the interchange of any pair of electrons, the spin-orbital, $\phi_i(x_i)$, concept is introduced [120].

$$\phi_i(x_i) = \phi_i(r_i) \cdot \sigma$$

Equation 27 – Spin-orbital as function of the product between an orbital wave function and spin function α or β.

The correction introduced in **Equation 27**, that was imposed in order to assure the Pauli exclusion principle, enables the usage of the spin-orbitals instead of the spatial orbitals described in **Equation 26**. It is important to notice that just the use of the spin-orbitals are not enough to achieve a fully antisymmetric system. The normalization of the different wave functions is achieved by arranging the spin-orbitals in a Slater determinant (**Equation 28**).

$$\Psi_{Hartree}(x_i) = \frac{1}{\sqrt{N!}} \begin{vmatrix} \phi_1(x_1) & \cdots & \phi_n(x_1) \\ \vdots & \ddots & \vdots \\ \phi_1(x_n) & \cdots & \phi_n(x_n) \end{vmatrix}$$

Equation 28 – Slater determinant.

The Slater determinant is based on the regular Fock matrix that contains the different spin-orbital of each of the N electrons present in the system. It is completely antisymmetric to any interchange of any pair of electrons, because if any two spin-orbitals have the same spin; then the rows that correspond to that spin-orbital are equal, and the resulting determinant is null due to having two columns in common [121]. As a result of the application of this theory, the Hartree-Fock equation can be written as described in the **Equation 29**.

$$\hat{F}_i \phi_i = \varepsilon_i \phi_i$$

Equation 29 – HF equation for the description a single electron of a spin-orbital ϕ_i.

The Fock operator is a specific operator associated to each electron and is defined by the Coulomb ($\hat{J}$) and exchange ($\hat{K}$) operators, as described in the next equation:

$$\hat{F}_i = \hat{h}_i + \sum_{j}^{N} (\hat{J}_{ij} - \hat{K}_{ij})$$

Equation 30 – Fock operator calculation for each electron.

The Hamiltonian $\hat{h}_i$ characterizes the electron i and it is composed by the sum of the kinetic energy of the electrons ($\hat{T}_N$) and the interactions between nuclei and electrons ($\hat{V}_{MN}$). The Coulombic operator, $\hat{J}$, is responsible for the repulsion between the electrons of the system, and the exchange operator, $\hat{K}$, for the correction of the energy that is related with the effects of spin correlation. In other words, since the Fock operator is described as a cumulative sum of the operators, the exchange operator corrects the electron-electron repulsion factor, when the same electrons recombine [120].

Within the Hartree-Fock methodology it is necessary to determinate the Fock operators ($\hat{F}_i$), and subsequently the form of the spin-orbitals monoelectronic function (ϕ_i) has to be known, as the bielectronic components ($\hat{J}_{ij}$ and $\hat{K}_{ij}$) of these operators, are dependent on the electronic density associated with the other electrons, *i.e.* the respective spin-orbital function, ϕ_k; $k \neq i$. With that being said, these functions are obtained by the resolution of HF equation, which require the Fock operators to be known. This problem leaded to the development of different iterative methodologies, as for example the self-consistent field (SCF). In this approach, it is supposed that the spin-orbitals of all the other electrons are known so when the calculation starts, approximate spin-orbitals based on the initial molecular structure are used. At the end of this first round of calculation, we have a set of improved wave functions for all the electrons. The cycle of computation is performed until the convergence criteria is achieved, which results in good approximations to the true system energy value [121].

The HF model requires higher computational cost and the HF equation resolution is more complex due to the lack of the characterization of the electronic correlation, therefore semi-empirical methodologies can also be used. These differ greatly in the computational cost through the usage of certain parameters that are already know. These approximations lead to faster calculations and to the application for bigger compounds [120, 121]. The parameters used for the approximations can be obtained either by high accurate computational methods or by experimental data. Thus, the usage of these methodologies can be not fully correct since they either require accurate computational methods or are dependent on low accurate experimental results.

1.4   Density Functional Theory

The resolution of the Schrödinger equation has been proven to be significantly hard to depict for large systems, thus a new approach based on the total electronic energy and the electron density profile was introduced. This methodology shows accuracy comparable to the *ab initio* and the application in bigger systems, while requiring lower computational cost and time.

The Density Functional Theory (DFT) was introduced in 1927, by Thomas and Fermi [122, 123], with the intention of simplifying the complex calculations of wave function theories using a physical observable: the electron density of the system (ρ). The integration of the electron density within all occupied space of the system gives the total number of electrons (**Equation 31**) [121].

$$N = \int \rho(r) \cdot dr$$

Equation 31 – Number of electrons present within the electron density of the system.

The total electron density of a system can be interpreted as a particular point in space r. Therefore, main advantage of the DFT approach is that the electron density is only dependent on three spatial coordinates (r), while remaining totally independent on the number of electrons that compose the system. In wave function-based theories, as the number of electrons in the system increase, an exponential increase in the complexity of the wave functions also occurs because they also accounted for the position, as well as the spin coordinate of each electron [124].

When we consider the electron density, the nuclei can also behave as a point charge, and they could be described as a local maximum in the electron density. The nuclear atomic number can be determined using this property, as the electron density maximum will be equal to the electron density of the corresponding atomic number, through the relation found in **Equation 32** [120].

$$\left.\frac{\partial \bar{\rho}(r_A)}{\partial r_A}\right|_{r_A=0} = -2 \cdot Z_A \cdot \rho(r_A)$$

Equation 32 – Electron density for an atomic nucleus A with atomic number Z_A and an averaged density $\rho(r_A)$.

In wave-based theories, the electronic description of the system is given by the square of the wave function integrated over $N-1$ electron coordinates. From **Equation 25**, for a system of M nuclei and N electrons, the electronic Hamiltonian within the Born-Oppenheimer approximation can be described as in the following equation:

$$\hat{H}_{el} = \hat{T}_N + \hat{V}_{MN} + \hat{V}_{NN} = -\frac{1}{2}\sum_{i=1}^{N}\nabla_i^2 - \sum_i^N\sum_A^M\frac{Z_A}{r_{iA}} + \sum_{i-j}^N\frac{1}{r_{ij}}$$

Equation 33 – Electronic Hamiltonian based on the Born-Oppenheimer approximation.

Therefore, the electronic Hamiltonian depends on the total number of electrons and the potential created by the nuclei, $\hat{V}_{NN}$, *i.e.* the nuclear charges and positions [120]. This means that according with the DFT formalism it is possible to build a Hamiltonian using the electron density function.

1.4.1 The Hohenberg-Kohn Theorem

In 1964, the DFT methodology was established based on the Hohenberg-Kohn theorems [125]. In their work, they defined two different theorems, in which the first demonstrates that in a non-degenerated system, the ground-state energy is defined by the electron density [124].

In the first theorem, they demonstrated that as the electrons interact with two different external potentials, $\hat{V}_{ext}$ and $\hat{V}'_{ext}$, it is observed the same electron density, ρ. Two different potentials require that the Hamiltonian and the corresponding ground-state energy wave functions are also different, however both provide the same ground-state electron density. In other words, Hohenberg and Kohn demonstrated that for the ground state a correspondence between the electron density and the nuclear potential is achieved, which leads to a correspondence between the Hamiltonian and the energy also. The energy is then considered as a unique functional of the electron density, $E[\rho]$ [120].

The second Hohenberg-Kohn theorem proved that the electron density followed the variational principle. Thus, to any trial density, it is possible for the expecting energetic value to be predicted ($E[\rho_{trial}]$), and it will always give an energy value that is greater than the real ground-state energy ($E_0[\rho_0]$), unless it is equal to it (**Equation 34**).

$$\langle\Psi_{trial}|\hat{H}|\Psi_{trial}\rangle = E[\rho_{trial}] \geq E_0[\rho_0] = \langle\Psi_0|\hat{H}|\Psi_0\rangle$$

Equation 34 – Energy calculated using a trial density function is equal or greater to the ground-state energy.

The definition of these theorems enabled the confirmation of the existence of the relation between the electron density and the energy of the system, but do not indicate the path that should be used to obtain the best density functions.

1.4.2 The Kohn-Sham Theory

The usage of orbitals in DFT methods in computational chemistry was introduced by Kohm and Sham in 1965 [126]. In this work, they presented a way to obtain the system energy by utilizing the density function. The Kohn-Sham (KS) formalism revolves around the calculation of the kinetic energy of the system in two parts, one which can be obtained exactly and small correction term accounting for electron-electron interaction [120, 124]. The KS methodology is similar to the HF method as it shares identical formulas of the kinetic, electron-nuclear and Coulombic electron-electron repulsion energies.

Applying the KS method, the exact ground-state energy density is not known, but it can be written as a sum of the auxiliary one-electron functions: the orbitals.

$$\rho(r) = \sum_i^N |\phi_i{}^2|$$

Equation 35 – Electron density definition.

The orbital formulation allowed the description of a hypothetical system, in which the electrons do not interact with each other. With this approach, the electron density of the system is identical to the ground-state density and the energy can be obtain by the sum of all the individual electronic kinetic energies (**Equation 36**).

$$E[\rho(r)] = T_s[\rho(r)] + V_{MN}[\rho(r)] + V_{MN}[\rho(r)] + E_{XC}[\rho(r)]$$

Equation 36 – Energy calculation using the KS theory.

The kinetic energy used, $T_s[\rho(r)]$, is an approximation to the real kinetic energy because it only accounts for non-interactive electrons. This term is corrected in the exchange-correlation term, $E_{XC}[\rho(r)]$, as it is composed by the correction to the kinetic energy from the interaction nature of the electron and all the non-classical corrections to the electron-electron repulsion energy. Even though the kinetic energy determined by this method is only calculated by assuming these non-interacting orbitals, the difference between the energetic value provided by HF and this method is not significative [120]. Calculations that use this methodology are difficult to perform due to the description of exchange-correlation term, since it is not known how to obtain it exactly [121, 124].

With that being said, the energy of the real system using the KS orbitals can be described as the following equation:

$$E[\rho(r)] = -\frac{1}{2}\sum_i^N (\langle \phi_i|-\nabla^2|\phi_i\rangle) - \sum_i^M \left\langle \phi_i \left| \frac{Z_A}{r_{1A}} \right| \phi_i \right\rangle + \frac{1}{2}\sum_{i-j}^N \left\langle \phi_i \left| \frac{\rho(r_j)}{r_{ij}} \right| \phi_j \right\rangle + E_{XC}[\rho(\vec{r})]$$

Equation 37 – Energy of the system using the KS orbitals.

The application of the variational principle is also used in this methodology, in order to obtain more easily the orbitals that approximates the density to the ground-state. This leads to the establishment of the Kohn-Sham equations (**Equation 38**), in a similar way to the HF equations [121].

$$\widehat{H}^{KS}\phi_i = \varepsilon_i \phi_i$$

Equation 38 – Orbital description using the KS equation.

The Kohn-Sham one-electron operator presented in the latter equation can be described as following:

$$\widehat{H}^{KS} = -\frac{1}{2}\nabla^2 - \sum_A^M \frac{Z_A}{r_{1A}} + \int \frac{\rho(r_2)}{r_{12}} dr_2 + V_{XC}(r_1)$$

Equation 39 – KS mono-electronic Hamiltonian.

The latter part of **Equation 39** is a functional derivative of the exchange-correlation term (**Equation 40**), thus it is unknown and requires to be approximated [121].

$$V_{XC} = \frac{\delta E_{XC}}{\delta \rho}$$

Equation 40 – Description of the functional derivative, V_{XC}.

1.4.3 Exchange-Correlation Functionals

DTF methods depend on a technique that facilitates the exchange-correlation term, $E_{XC}[\rho(r)]$, to be approximated to the real value. The type of approximation that is used for this exchange-correlation functional is the main source of inaccuracy in DFT [124]. This term can be separated into different functionals: the exchange functional, $E_X[\rho(r)]$, that considers only the interaction between electrons with the same spin; and the correlation function, $E_C[\rho(r)]$, that involves electrons of opposing spin [120]. In order to obtain these functionals, several approximations were introduced.

The local density approximation (LDA) considers that each electron feels a uniform and continuous distribution of the electron density, regardless their position, *i.e.*, the exchange-correlation energy is obtained per electron in a homogeneous electron gas of constant density (**Equation 41**) [120].

$$E_{XC}[\rho] = \int \rho(r) \cdot \varepsilon_{XC} \cdot [\rho(r)] \cdot dr$$

Equation 41 – Exchange-correlation energy calculation using LDA.

The first time this approximation was introduced in 1930, Paul Dirac [127] proposed that the exchange energy functional could be expressed as:

$$E_X[\rho] = -C_X \int \rho^{4/3}(r) \cdot dr$$

Equation 42 – Exchange energy for a uniform electron gas according to the Dirac formula.

This approach was surprisingly accurate for idealized metal systems; however due to the crude nature of the approximations, it was very dependent on an accurate electronic density, that leaded to the inaccurate description of systems where the density is not distributed uniformly or with an high number of molecules [120, 121].

In order to correct this flaw and extend this to open-shell systems, Slater [128] introduced the spin dependence into the functionals. The local spin-density approximation (LSDA) can be characterized by the difference between the spin-up and the spin-down electron density, ρ_α and ρ_β respectively (**Equation 43**) [120, 124].

$$E_X[\rho] = -2^{1/3} \cdot C_X \int \left[\left(\rho_\alpha{}^{4/3} + \rho_\beta{}^{4/3} \right)(r) \right] \cdot dr$$

Equation 43 – Exchange energy calculation using LSDA.

This extension that is dependent on the spin and the total electron density allows the investigation of the magnetic structures of metals and alloys [121]. These two last approaches consider a homogeneous electron gas, which is far from ideal as any real system contains varying electron density through all the system. The generalized gradient approximation (GGA) methods were the first to introduce the first derivative of the density, $\nabla\rho$, as a variable into their description. These methodologies are derived also take into consideration the spin, as LSDA, and introduce another correction to the system, *i.e.*, it is required that Fermi and Coulomb holes, are integrated to -1 and 0, respectively [120]. The GGA methods are calculated in a very similar way to LSDA, however they account for a density gradient (**Equation 44**).

$$E_{XC}[\rho] = -2^{1/3} \cdot C_X \int \left[\left(\rho_\alpha{}^{4/3} + \rho_\beta{}^{4/3} \right)(r) \right] \cdot dr + \frac{|\nabla\rho(r)|}{\rho(r)^{4/3}}$$

Equation 44 – Exchange-correlation energy calculation using GGA.

This methodology as proven to be an accurate and efficient method for the calculation of *d*-metal complexes [121]. GGA approximations can also be improved if we consider the higher derivatives of the electron density, *i.e.*, the introduction of the Laplacian of the electron density, $\nabla^2\rho$. These higher order gradient, or meta-GGA

methods, can instead account for the orbital kinetic energy density (τ) which are derived from the occupied KS orbitals [120, 124].

An overview of the exchange-correlation functional described in this work and examples of their application can be found in **Table 1**.

Table 1 – Overview of the exchange-correlation functionals.

Name	Variables	Examples
Local density	ρ	LDA, LSDA
GGA	ρ and $\nabla\rho$	B88 [129], P [130], PW91 [131], LYP [132]
Meta-GGA	ρ, $\nabla\rho$, $\nabla^2\rho$ or τ	B95 [133], KCIS [134], TPSS [135], VSXC [136]

The functionals referred above proved to be a good approximation tool for computational chemists to calculate in a rigorous way the exchange-correlation function of DFT. Later down the line, hybrid functionals were developed and they allowed a significant increase in performance, when compared with GGA for many molecular properties [124]. This hybrid methodology combines the exchange-correlation of a conventional GGA method with the Hartree-Fock exchange functionals (**Equation 45**).

$$E_{XC}{}^{hybrid} = aE_X{}^{HF} + (1-a)E_{XC}{}^{DFT}$$

Equation 45 – Hybrid exchange-correlation energy calculation.

Among the hybrid functionals, B3LYP is by far the most popular in computational chemistry [124]. It is a hybrid-GGA method that combines the three-parameter Becke functional (B3) [137] and the LYP functional [132] with some HF exchange terms (**Equation 46**).

$$E_{XC}{}^{B3LYP} = aE_X{}^{HF} + (1-a)E_X{}^{LSDA} + b\Delta E_X{}^{B88} + (1-c)E_C{}^{LSDA} + cE_C{}^{LYP}$$

Equation 46 – B3LYP exchange-correlation energy calculation.

The a, b and c parameters are determined by fitting to experimental data, and typically $a \approx 0.2$, $b \approx 0.7$ and $c \approx 0.8$ [120]. This functional is one of the more commonly used since it represents one of the most successful in overall performance. However, it demonstrates decreasing accuracy with an increase in the system size, and usually underestimates the energy of non-covalent interactions. Thus, this functional provides good enough results that are very close to the experimental value and the energy calculation error normally obtain is < 3 kcal·mol^{-1} [138].

There has been a focus around increasing the performance of the B3LYP functional, however this has not been able to be achieve due to the fact that by tailoring the functional form or the addition of more fitting parameters, results in the deterioration of the results of other properties [120].

In this work, there is a need for describing with accuracy all types of interactions, *i.e.*, both intra and intermolecular interactions due to the permeation studies and the hydrogen bonds that are predicted to be formed in our system. As referred above, the B3LYP functional fails to describe accurately some intermolecular interactions, therefore as an alternative it was decided to use the M06-2X functional. This functional has been proved to outperform B3LYP in several different systems that include non-covalent interactions [139].

M06-2X belongs to the family of Minnesota functionals developed by Truhlar in 2007 [140, 141]. This functional is a meta-GGA hybrid functional and is derived of its counterpart the M06. This functional was introduced with 54 % of Hartree-Fock correction and it also combines the PBE exchange functional [142] with the B97 correlation functional [143] (**Equation 47**) [140].

$$E_{XC}{}^{M06} = 0.54 \cdot E_X{}^{HF} + 0.46 \cdot E_X{}^{DFT} + E_C{}^{DFT}$$

Equation 47 – M06-2X exchange-correlation energy calculation.

1.5 Basis Sets

Basis sets are another possible way to achieve higher levels of accuracy of the DFT methodology as these are sets of mathematical functions used to describe atomic orbitals in quantum mechanical calculations. In order to achieve better and more accurate results, it is required to utilize a larger basis set, as it describes more optimally the electron density. If there was enough computational power, we could achieve a very good description of the system in study with the usage of an infinite number of basis sets. In order to achieve computational efficiency, there is a need to find a compromise between accuracy and computational cost. These functions need to be able to describe the real wave function and provide good results, while solving the exchange-correlation functionals without an excessive computational cost [120, 121]. The mathematical functions that are used to characterize the atomic orbitals can be divided into two categories, and these will be described briefly in this section.

1.5.1 Slater type orbitals

Slater basis sets were the first to be introduced to describe the electron density around an atom. The Slater type orbitals, STOs, have an exponential dependence of the nucleus-electron distance, that reflects the behavior of the hydrogen atom orbitals. The exponential dependence assures a fast and simple convergence process, however the calculation is limited to systems with a few number of atoms due and the calculation of the three- and four-center two-electron integrals can be impossible to perform. This leads to STOs being normally used in mono or diatomic systems [121].

1.5.2 Gaussian type orbitals

The introduction of the Gaussian type orbitals (GTOs), played a major role in making the calculations more feasible as the GTOs are the most used types of basis sets and they bypass the STOs limitation by replacing the e^r dependence by a e^{r^2}. The definition of the Gaussian functions are as follows [121]:

$$\chi_{xyz;\alpha ijk}{}^{GTO}(r_1 - r_c) = (x_1 - x_c)^i \cdot (y_1 - y_c)^i \cdot (z_1 - z_c)^k \cdot e^{-\alpha|r_1 - r_c|^2}$$

Equation 48 – GTO function, in which r_1 are the coordinates of the electron (x_1,y_1,z_1) and r_c are the coordinates of the center of the Gaussian function (x_c,y_c,z_c).

In the latter equation, (i,j,k) are non-negative integers that are used to define the orbital nature, and α is used to determine the width of the GTO. GTO is an *s*-type orbital when all integers are equal to zero; when the one of the integers equals one, there is present an *p*-type orbital; and when $(i + j + k = 2)$ it is obtained a *d*-type orbital. GTOs functions solve the problem for the two-electron integrals in STOs, due to the product of two different Gaussians at different centers is equivalent to a single Gaussian function centered between the two centers, that allow integrals on three- or four- atomic centers to be reduced to only two, making calculations much easier. However, due to its r^2 exponential dependence they give a poorer representation of the orbitals at the atomic nuclei. Therefore, to achieve the same accuracy as the STOs, normally GTOs are grouped together. This is known as the contracted GTO functions (CGTO) and they are considered to be a fixed combination of the original GTOs and the orbitals are written in the next equation [120, 121].

$$\phi_i = \sum_j^M c_{ji}\chi_j$$

Equation 49 – The molecular orbitals are expressed as a linear combination of the CGTOs.

These functions allow the improvement in the description of the electrons close to the atomic nuclei, while not diminishing the results quality.

With that in mind, there is the possibility to construct CGTOs in several different ways. For example, the expansion of the STO in terms of the N primitive GTOs that are used are defined as STO-NG, being the most commonly used the STO-3G. This CGTO approach is considered a single-zeta basis set, as it only uses one basis function for each orbital. It is possible to contract the different basis function using more primitives for each orbital, leading to a multi-zeta basis set [121]. Even though the usage of more basis functions leads to better accuracy, it also leads to an increase in complexity of the calculations.

In order to achieve a compromise between accuracy and computational cost, and with the knowledge that the valence orbitals are more influenced by other atoms when compared with core orbitals, Pople introduced the split-valence basis concept. This approach treats the core orbitals with a specific number of Gaussian primitives, and the valence orbitals with a higher number of functions. This approach is widely used and have the form n-abcG, in which n represents the number of the contracted GTOs for description of the core orbitals, and abc represents the number of basis functions used for the valence orbitals [120, 121]. As an example of this, the most common basis set used in research, 6-$31G$ applies six primitive GTOs for the core orbitals and three primitives for the more internal valence orbitals and one for the external ones.

This approach can correctly characterize isolated atoms, however it can undervalue some interactions in molecular systems where polarization of the bonds stablished are considered, *e.g.*, one of the *p*-orbitals of the hydrogen atom can polarize the *s*-orbital, distorting the normal bond that is formed [120]. Pople introduced the polarization functions and their notation appears after the G, and uses the notation d for the *d*-functions that are added to polarize the *p*-orbitals that are present in heavy atoms, and uses p for *p*-functions that are used to polarize the *s*-orbitals of the hydrogen atoms, *e.g.*, 6-$31G(d)$ and 6-$31G(d,p)$, respectively [120, 121]. Pople GTOs, can also neglect some situations where the electrons are loosely bound, *i.e.*, in cases where highly negative or polarized molecules displace the electron density in relation with the nucleus. This would lead to less accurate description of this cases, therefore Pople introduced the concept of diffuse functions. These always appear before the G and their notation is the addition of a "+" or "++" if they assigned the diffusion functions to heavy atoms or heavy and hydrogen atoms, respectively.

1.6 Solvation Models

The methods for calculation referred until this point, only take into consideration molecules in a vacuum ambient, *i.e.*, in an isolated state. This completely neglects the effect of the environment that the molecules are inserted, which can lead to a misjudge in the energies of the system since the surrounding environment can change the properties of the system, *e.g.*, solute in a solvent.

There are two possible approaches for evaluating the solvent effect and they could be derived in two different types, those who add solvent molecules to the system and treat them individually; and those who threat the solvent as a continuous medium. The latter is the most commonly used, even though it models the solvent in a less rigorous fashion due to the other methodology being computationally expensive, since they require an explicit description of the solvent molecules and interactions.

The continuum models aim for the description of the solvation process by considering the solvent as a homogeneous medium with a dielectric constant, thus producing an electrostatic stabilization to the system that permits the calculational of the solvation free energy (**Equation 50**) [144].

$$\Delta G_{solvation} = \Delta G_{dis} + \Delta G_{cav} + \Delta G_{el} + \Delta G_{rep} + \Delta G_{Mm}$$

Equation 50 – Calculation of the solvation free energy.

The term ΔG_{dis} in the latter equation account for the solute-solvent dispersion interactions; ΔG_{cav} account for the energy needed to form the molecular cavity inside the continuum representing the solvent; ΔG_{el} is the electrostatic interaction between the solute and the solvent that comes from the polarization in the charge distributions; ΔG_{rep} is the repulsion energy; and ΔG_{Mm} accounts for the molecular motion and for the entropic contributions to the Gibbs free energy.

The model that is used for this work employs the Polarizable Continuum Model (IEF-PCM), and with it is possible to obtain a detailed description of the electrostatic potential by a correct parametrization of the cavity and the dispersion contributions based on the surface area.

D. RESULTS AND DISCUSSION

"It pays to keep an open mind, but not so open your brains fall out".

Carl Sagan

As referred before, the creation of membranes for separation processes could be a sustainable alternative either to the conventional technologies based on phase transitions that require a significant energy cost to the separation; or to combat the scarcity of fresh water due to the creation of an appropriate desalination process of the sea water.

In the present work we studied the permeation of gases and ions in solution through graphene nanowindows using DFT calculations. The results that were obtained can be compared with literature reports that used MD simulations. This chapter initial focus is based on the initial characterization and proper preparation of the system, as well as, the proper selection of both the functionals and the basis sets in order to parametrize the following studies, *i.e.*, the permeation of molecules through the graphene membranes.

1. Model preparation

In order to perform this study, we started with a pristine graphene layer that was created with the *GaussView 5.0.8* software [145]. This initial sheet was square-shaped, containing 336 atoms, in which 290 were carbon atoms and 46 hydrogen atoms on the edges of the graphene layer. With the creation of this framework, an adequate preparation of structures that are reported in the literature were generated [5, 96]. These membranes contained different functionalizations and different shaped nanowindows that can change the size of the hole and allow the permeation of gases through them (**Figure 12**). For example, the addition of a hydroxyl group improves the affinity with the permeating molecules and the addition of an ether group allows for the nanowindow to increase in size.
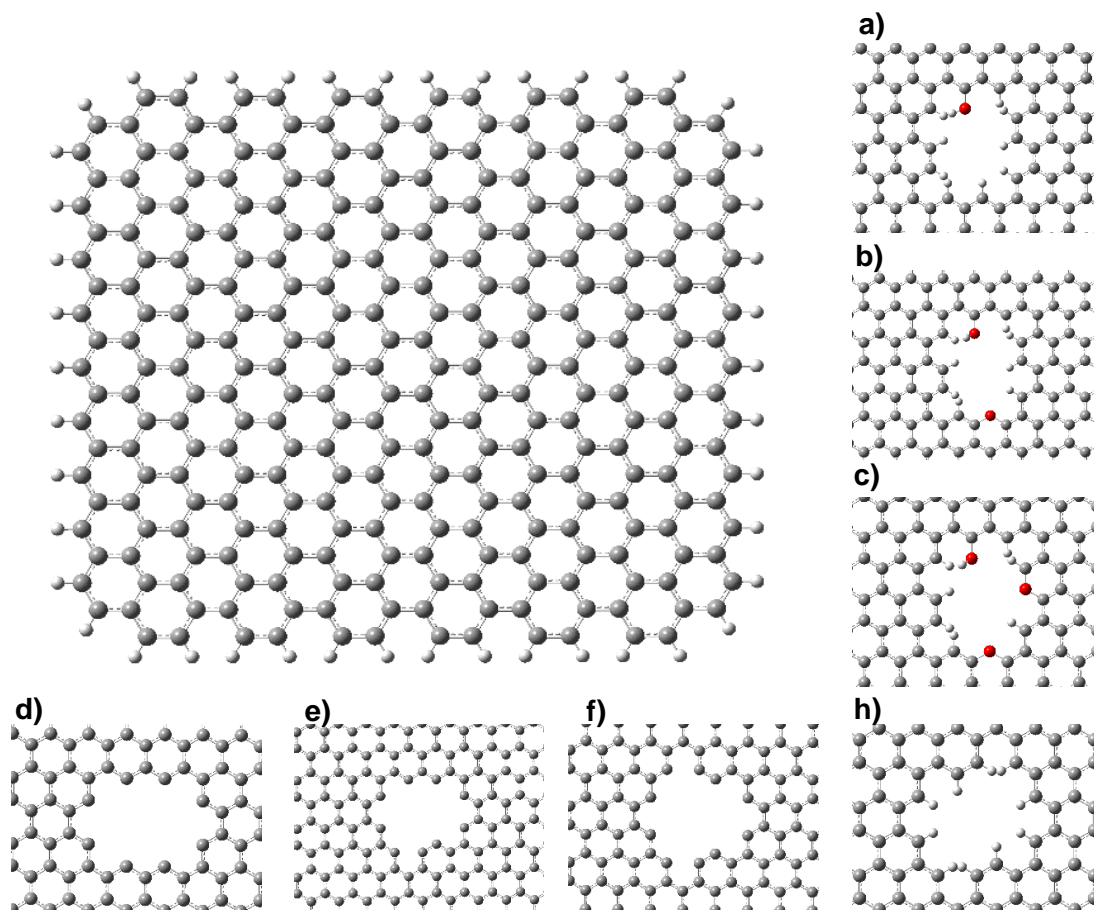
Figure 12 – Initial model created; a) Vallejos-A hole, b) Vallejos-B hole, c) Vallejos-C hole, d) H2N2-A hole, e) H2N2-B hole, f) H2N2-C hole, h) Vallejos-onlyh-AB hole.

Afterwards, a DFT study of these different systems was performed using the B3LYP functional and as basis set the SLDB approach, where some atoms in the system are treated with a low basis, 3-21G (outer atoms of the membrane); and the remaining with an higher basis, 6-31++G(d,p) (atoms that are in the nanowindow-rim and the ones close to them). With this approximation, even though a low description of the outer membrane is achieved, it is possible to describe with higher accuracy the nanowindow-rim chemistry without compromising the computational time.

Despite the effort to perform these calculations with this approach, through the creation of several different input files, in all the obtained calculations the optimization never ended without errors being observed. Upon the observation of these calculations with errors, we concluded that the error is possibly due to the higher basis set that is being used; and that the computational time required for the calculation was too high, *ca.* 3 days (cpu time).

With these remarks from the first procedure, an optimization of the initial system was performed and the pristine graphene framework was reduced to 274 atoms, *i.e.*,

232 carbon atoms and 42 hydrogen atoms, in order to reduce the computational time (**Figure 13**).

Figure 13 – Representation of the change in Vallejos-A hole using the quadrangular approach; a) and b) differ in the number of atoms and the shape of the model.

In these DFT calculations, we used the B3LYP functional and as basis set, two different selections were carried out. On one hand, to check whether the size of the basis was a problem or not, we used the same approach as before, the SLDB; on the other hand, in order to have a full optimization in which we could control the computational time that is required for preliminary geometry determinations, we used the STO-3G basis set applied to the full system. As expected, the output files that were related with the SLDB basis set resulted in errors, which confirmed the theory that the higher basis set used in these calculations do not allow the optimization to occur.

Considering the results using STO-3G as the basis set, it was possible to obtain the first optimizations without any error occurring. These calculations took roughly 2.5 days of cpu time and originated the first geometry for the membranes in study, and the assigned energies for each model are indicated in **Table 2**. With the analysis of the output files it is possible to observe that the membranes with higher functionalization tend to bend in order to minimize their energy (**Figure 14**). As reported in the literature, graphene sheets can assume some type of bending [74], thus if there was a big difference, we would be unable to correlate our results with a full graphene sheet, *i.e.*, our smaller sized structure can have a different behaviour, as it is used to compare with a graphene sheet with limitless range.

Table 2 – Energies obtained to each optimized structure; Vallejos-B and Vallejos-C holes, are demonstrated in Figure 14- a) and b), respectively.

Energies obtained for the optimized structures / 10^7 kJ·mol^{-1}	
Vallejos-A hole	-2.163
Vallejos-B hole	-2.172
Vallejos-C hole	-2.181

a)   b)
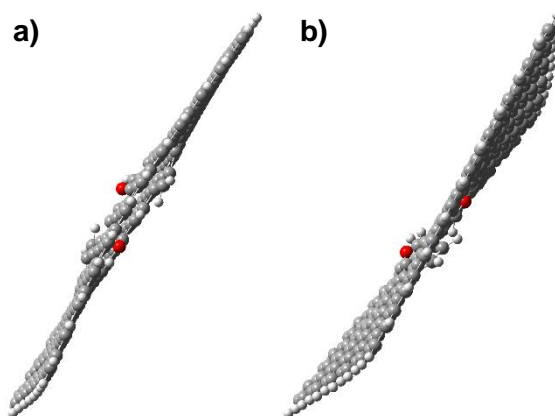
Figure 14 – Optimized geometries, using the quadrangular approach, of a) Vallejos-B and b) Vallejos-C holes.

As a consequence of these results and in order to continue with the study, some changes were promoted to minimize the bending that was observed and the computational time required for a higher optimization, *e.g.*, the use of a higher basis set and a different functional. In order to minimize the system repulsion and distortion, while maintaining the correlation with a bigger membrane, the framework was adapted to the shape of a cyclohexane (an hexagonal approach), which resulted in a smaller structure with 220 atoms, composed by 176 carbon atoms and 44 hydrogen atoms (**Figure 15**). These change in the shape and size of the membrane is expected to also reduce the cpu time required for further and higher optimizations.
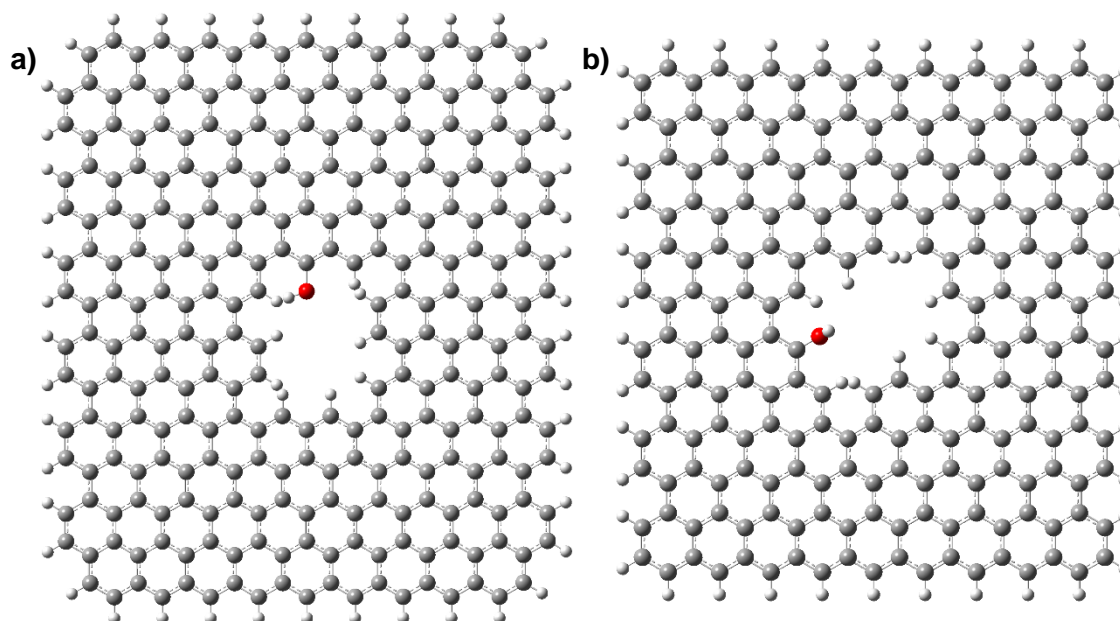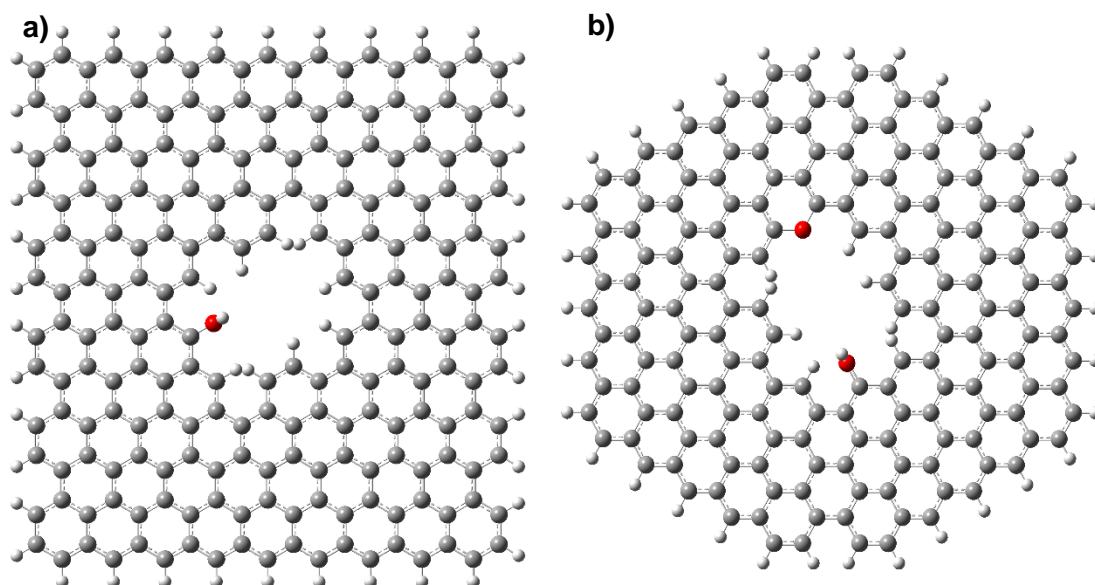
Figure 15 – Representation of the change in Vallejos-B hole, using the hexagonal approach; a) and b) differ in the number of atoms and the shape of the model.

Similarly to the procedure used before, a DFT study of these new membranes was performed using M06-2X as functional and STO-3G as the basis set. As expected, this study took a lesser amount of time to finish, *e.g.*, 1.95 days of cpu time; and it was possible to obtain the geometries for this new hexagonal approach to the membrane. The resulting optimized energies for these membranes are shown in **Table 3**.

Table 3 – Energies obtained to each optimized structure; Vallejos-B and Vallejos-C holes, are demonstrated in Figure 16- a- 1) and a- 2), respectively.

Energies obtained for the optimized structures / 10^7 kJ·mol^{-1}	
Vallejos-A hole	-1,766
Vallejos-B hole	-1,776
Vallejos-C hole	-1,785

Taking into consideration the new geometries, it is possible to compare them with those that resulted from later calculations, *i.e.*, the linear framework shown in **Figure 14**. As it is observed (**Figure 16**), the hexagonal approach shows a smaller bend comparing with the linear approach for both membranes with higher functionalization while maintaining an optimal size for correlation with an unlimited pristine graphene sheet.
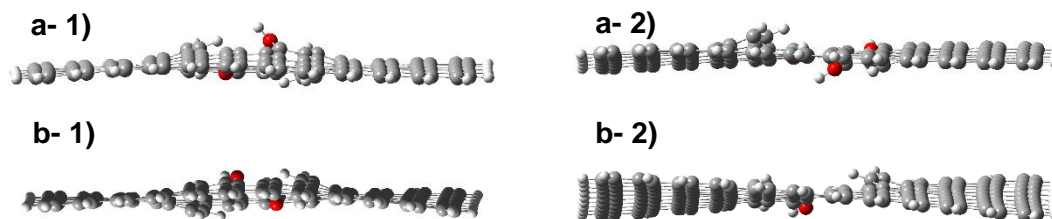
Figure 16 – Comparison between optimized geometries, using the a) hexagonal approach and using the b) quadrangular approach, of 1) Vallejos-B and 2) Vallejos-C holes.

In order to recognize more easily the difference in warping or undulation observed between the different approaches, an analysis of the literature was performed. The study of the undulation observed in membranes that is presented in the literature, is normally related to lipid membranes and MD simulations, being the first method applied the thermal undulation spectrum (TMS) [146]. Other alternatives are available in the literature [147], however those methods are not specific to our model in study. To perform this analysis the root-mean-square deviation (RMSD) of atomic positions between the membrane and the z-plane (**Equation 48**) was performed and the results obtained are eventuated in **Table 4**.

$$RMSD = \sqrt{\frac{1}{n}\sum_{i=0}^{n}(Z_{ref} - Z_i)^2}$$

Equation 51 – RMSD between the membrane and the z-plane (z=0).

Table 4 – Study of the undulation observed in the membrane through the calculation of RMSD of the atomic positions between the membrane and the z-plane, for the quadrangular and the hexagonal approach.

Study of the warping observed in the membrane		
Vallejos-A hole	0.403	0.343
Vallejos-B hole	0.373	0.366
Vallejos-C hole	0.520	0.329
	Quadrangular approach	Hexagonal approach

Considering the geometries observed in the **Figure 5**, it is possible to recognize that the bending observed in the membrane is smaller when the hexagonal approach is performed. This conclusion is verified by the results obtained from the RMSD calculation (**Table 3**), as it is possible to see that the hexagonal approach has an overall smaller deviation from the z-plane than the quadrangular approach. Taking into consideration the result of the undulation observed and the cpu time required to perform these optimizations, we concluded that the hexagonal approach was the best method to create the different membranes that we want to study.

2. Definition of the models

In order to proceed with the study of the permeation of gases and ions through the membranes created with the hexagonal approach, the normalization of different parameters is needed to be performed.

2.1 Optimization states

As previously mentioned, in this study a comparison between a finite and smaller membrane and a full graphene sheet is performed. Therefore, in addition to the best approximation possible with the model described before it is needed to take into consideration different optimization states (**Figure 17**). The usage of these different states is also an important tool to correlate our results with the literature since it contains several studies, mostly MD simulations, in which the nanowindow assumes no protonation in the nanopore edge and too idealized symmetries [96, 99], as well as the lack of any heteroatom [96, 101, 102]; and the usage of an rigid membrane framework [97, 100, 101].

The optimization states that were taken into consideration in this study differ in the atoms that are unable to move during the optimization procedure. For one of the states it is allowed the atoms to optimize without any restriction, resembling a flexible membrane (*nof*), whereas the others have the outer rim of the nanowindow frozen, which leads to a rigid membrane. The only difference between the latter, is that the hydrogens atoms in the outer membrane are freely to move (*foutnoh*) and in the other case the hydrogens are frozen (*fallout*). It is not expected to exist any difference in the shape of the membrane between these last states, they are taking into consideration because the cpu time required to optimize both can differ. In **Figure 17** are highlighted in blue which atoms in the membrane are frozen, in order to clarify the difference between each state.
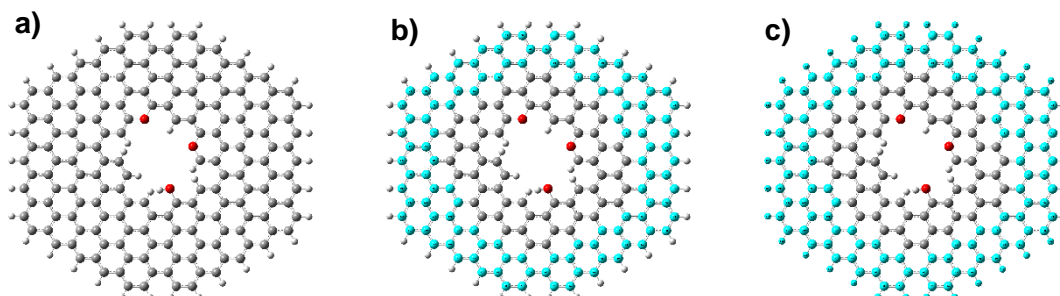
Figure 17 – Demonstration of the different optimized states on Vallejos-C hole, a) *nof*, b) *foutnoh* and c) *fallout*.

2.2 Theoretical description

In order to improve the veracity and the theoretical description of the system in study, an examination of which basis set and functionals that should be applied in all the further studies is performed.

Even though it is expected for the higher basis set, *i.e.*, with polarization and diffusion functions to achieve a lower and more specific energy, the cpu time required for the increase in performance can be considerable and it can neglect the progress of the work. This study is also important to check if it is possible for the calculation to achieve its conclusion, with the usage of these higher functions due to the size of the system in study. For this reason, a collection of functions that ranged from STO-3G to 6-31++G(d,p) were tested using the Vallejos-A hole and the *nof* state, and the results for the cpu time required for each basis set are shown in **Figure 18**. Concerning the x-axis, the unit assumed is cpu days per number of steps, since in order to reduce the time of this study the initial geometry obtained by STO-3G was used to get the remaining optimizations. In the y-axis the basis set are displayed in an increasing order that is related to the number of basis functions used.
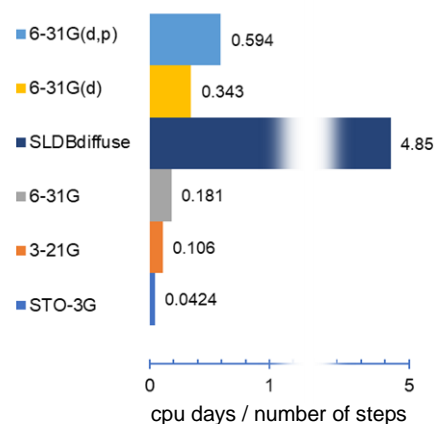
Figure 18 – Relation between the computational time required (in days) for each basis set that was studied.

As it is possible to see in the latter figure, diffuse functions, *e.g.*, 6-31+G(d) or 6-31++G(d), are not present due to the fact that the calculation was not able to achieve an normal termination when these basis set were used. In order to allow these types of functions to be possible to characterize our system, a QM/QM study was performed. The SLDB$_{diffuse}$ present in **Figure 18**, relates to these type of study in which the usage of two different basis set to describe different levels of optimization in the system, as the outer atoms of the membrane are treated using 3-21G and the atoms closer to the nanowindow are treated with 6-31++G(d). It is a similar approach than the one used in **Figure 17- c)**,

however in this case the highlighted atoms correspond to the outer and lower treated level.

According to the results obtained in **Figure 18**, it is possible to see that the usage of a higher amount of functions or even an increase in the number of primitives (the 6-31G and the 3-21G have the same number of functions) makes the calculation last longer. Therefore, for the continuation of this project a selection of the best basis set to apply in the study was made taking into consideration the system and the computational time required for each calculation. Our system is composed by several carbon and oxygen atoms thus the first polarization function is needed because it describes better the π-bonds that are established in the membrane. With this in mind, 6-31G(d) was the basis set that was choose for the continuation of the studies.

Furthermore, the test of the influence of the functionals used in the DFT calculations was also performed. In order to obtain these comparison we used a property related with Vallejos-B hole that it can have two different geometries that are stable, namely the open and closed conformation [5]. The difference between both is how the hydrogens duplets align in the nanowindow and it is evidenced in **Figure 19**.
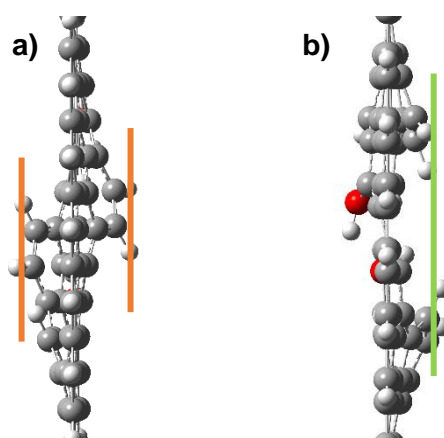
Figure 19 – Representation of the different conformations in Vallejos-B hole, a) open (duplets in opposite sides, highlighted at orange) and b) closed conformation (duplets in the same side, highlighted at green).

A calculation of the energetic difference and the analysis of the computational time required for the optimization between both conformations was the performed. In this case, B3LYP and M06-2X were used. As previously stated in this work, according with recent studies, M06-2X describe better the non-covalent interactions that are established in our system [139], therefore it is expect for this functional to reproduce the best optimization result. For this study, the Vallejos-B hole was optimized with STO-3G for both functionals and the resulting geometry was the open conformation. This geometry was then submitted for new calculations with the 6-31G(d) basis set. For the closed

conformation, we adjusted the latter geometry by moving the hydrogens towards the same side of the membrane and through a re-optimization we got the closed conformation geometry, as it corresponds to a local minima. Afterwards, an optimization using 6-31G(d) basis set for this conformation was also made. The results obtained can be found in **Table 5**.

Table 5 – Comparison of the functionals to use in this study using the energetic difference in the possible conformations of Vallejos-B hole.

Functionals in study	$\Delta E_{conformations}$ / kJ·mol^{-1}	mean cpu time per scan / days
B3LYP	1.549	0.724
M06-2X	1.993	0.793

These results obtained by the usage of these two different functionals show that the energetic difference calculated for B3LYP is smaller and that using it has the functional it is possible to have a smaller computational time per scan, even though it is only by a small margin.

Upon these results, we still choose the M06-2X for the functional to be used in subsequent studies due to all the reports that are present in the literature that show that this functional is better for the type of system that we are using in this work. M06-2X, showed a similar computational time required while describing better all the non-covalent interactions present in the graphene membranes. Previous work from our group also showed great premise using this functional for all the calculations [148].

3. Membrane characterization

All electronic structure calculations that were carried out after this point were performed using the hybrid exchange-correlation functional M06-2X and the 6-31G(d) Pople basis set.

3.1 Membrane optimization studies

As the starting point for this study, the membranes that are present in **Figure 20** were optimized using the different optimization states that were described in **Figure 17**. As said before, these calculations can be used as a starting point for the comparison of our results with the portrayed in the literature using MD calculations. The resulting geometries of the membranes with the different optimization states can be found in **Figure 21**. The difference between the geometry obtained for *fallout* and the *foutnoh* states is, as expected insignificantly, therefore only the comparation between *nof* and *foutnoh* is performed for all membranes in the latter mentioned figure.
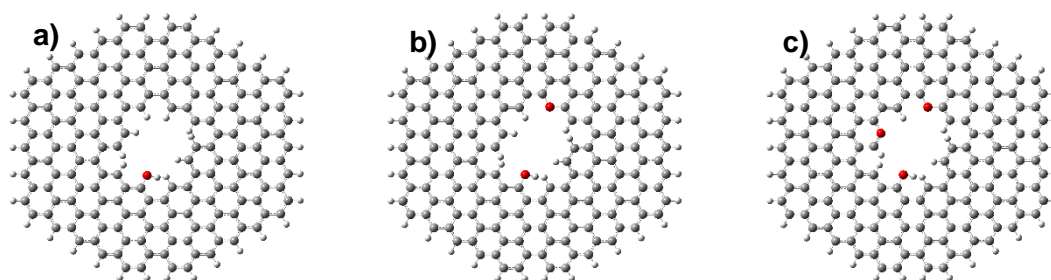
Figure 20 – Representation of the graphene membranes with different functionalization in study, a) Vallejos-A, b) Vallejos-B and c) Vallejos-C holes.
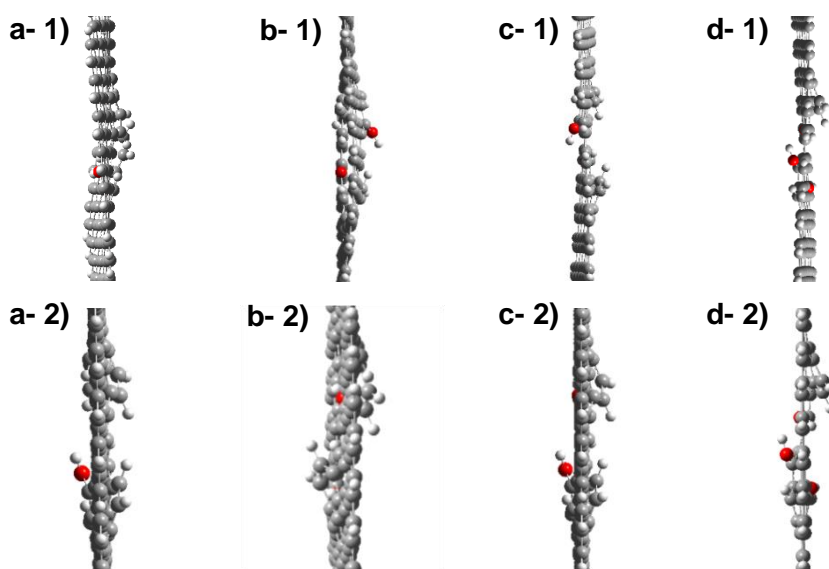
Figure 21 – Representation of the optimized geometries of a) Vallejos-A, b) Vallejos-B open, c) Vallejos-B closed and d) Vallejos-C holes obtained by using 1) *nof* and 2) *foutnoh* optimization states.

From the observation of the geometries obtained in **Figure 21**, it is possible to see that there is a clear distinction between the flexible and the rigid approaches. In these results, an unexpected outcome for the rigid optimizations appeared, due to the fact that the minimum conformational energy in Vallejos-B hole was the closed conformation, instead of the open that was obtained by the flexible approach. The energetic difference between the *nof* state and the freezed ones was calculated and the results can be found in **Table 6**.

Table 6 – Energetic difference between the different optimization states, using *nof* as the reference.

	Vallejos-A	Vallejos-B$_{open}$	Vallejos-B$_{closed}$	Vallejos-C
$\Delta E_{nof \rightarrow foutnoh}$ / kJ·mol^{-1}	329.5	317.7	308.4	316.5
$\Delta E_{nof \rightarrow fallout}$ / kJ·mol^{-1}	346.5	338.1	325.4	

With these results, it is possible to have a confirmation that letting the membrane optimize freely, without any restrictions, can result in a more stable membrane when comparing with the linear restriction in the membrane that are found in some MD studies. After this conclusion, a comparison between *foutnoh* and *fallout* states was also performed, in order to check if the hydrogen on the edges of the graphene membrane being restricted conduced to a different outcome in energy and in computational time. The energetic difference and the cpu time required for each calculation can be found in **Table 7**.

Table 7 – Energetic difference between the frozen optimization states for the different membranes in study.

Membranes in study	$\Delta E_{foutnoh \rightarrow fallout}$ kJ·mol^{-1}	mean cpu time per scan / days	
		foutnoh	*fallout*
Vallejos-A	17.0	0.360	0.368
Vallejos-B$_{open}$	20.5	1.036	1.068
Vallejos-B$_{closed}$	17.0	0.967	1.063

As it is possible to see from the data in the latter table, when the hydrogen atoms were used without any restriction, the computational time significantly reduced while maintaining nearly the same energy.

With these last two remarks, the *fallout* optimization state was discarded and for the next studies, the optimizations were performed with the other two states. The *nof* state, without any restriction and the *foutnoh* state, that had only the carbon atom that are external to the nanowindow unable to move (as it was referred and demonstrated in **Figure 17**). Due to the fact that only these two states are used after this point, it is possible to differentiate the *nof* state as the flexible membrane and the *foutnoh* state as the rigid membrane.

Before moving to the next step in our work, an important property of the system in study, that was already referred before, required our attention. The energetic difference between the different conformations in the Vallejos-B hole, present in **Table 6**, is a result that is present in literature [5]. Therefore, a comparison between our results and the literature was performed and can be found in **Table 8**.

Table 8 – **Comparison between the energetic difference observed in the different conformations of Vallejos-B hole with the literature, using both optimization states.**

	Ref. [5]	Flexible membrane	Rigid membrane
$\Delta E_{conformations}$ $kJ \cdot mol^{-1}$	1.3	1.99	7.25

We are comparing our results with the work performed by Vallejos *et al.* that is present in the literature. It is important to note, that their study is performed using MD simulations. With the data present in **Table 8**, it is possible to compare the difference between a DFT and a MD study.

3.2 Electrostatic potential maps

Electrostatic potential maps illustrate the charge distributions of molecules and allow the visualization of the size and shape of molecules in study. Therefore, this study it is important for this work because it can display the real size of the nanowindow in the different membranes that are being studied.

The unfreezed membranes that were optimized before, were submitted to this study and the resulting electrostatic maps are displayed in the next two figures. **Figure 22** demonstrates the main full electrostatic map with two different views for Vallejos-A hole; and in **Figure 23** it is evidenced the nanowindows size on the different membranes that were created, the outer electrostatic map is similar to the ones demonstrated in **Figure 22**.
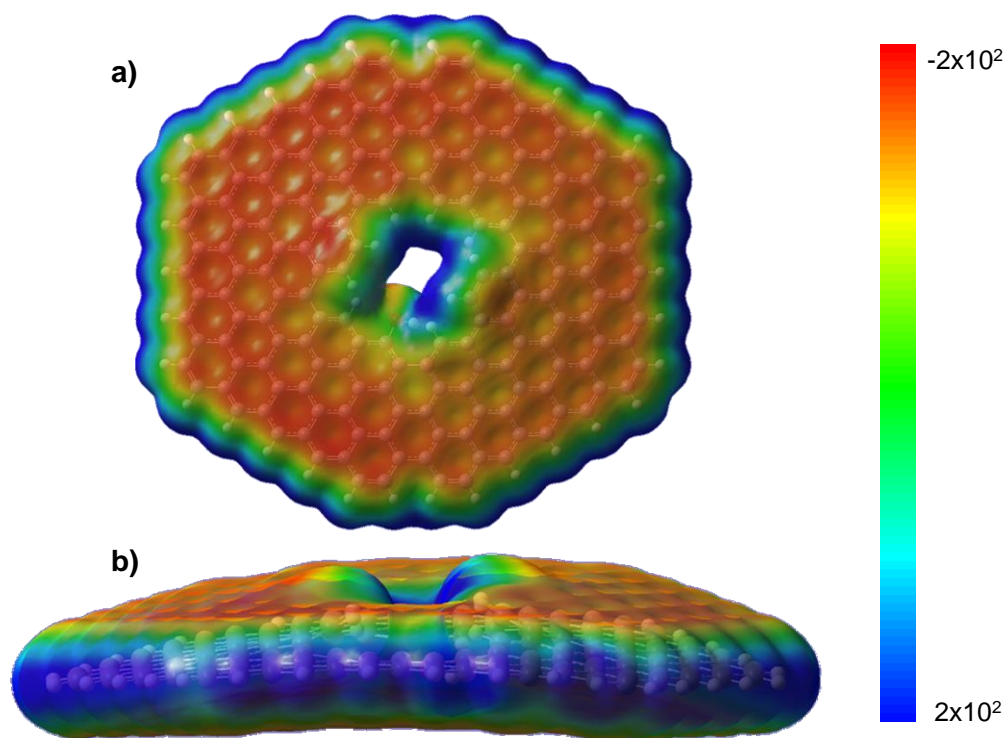
Figure 22 – Electrostatic potential maps of flexible Vallejos-A hole; a) front-view and b) side-view.
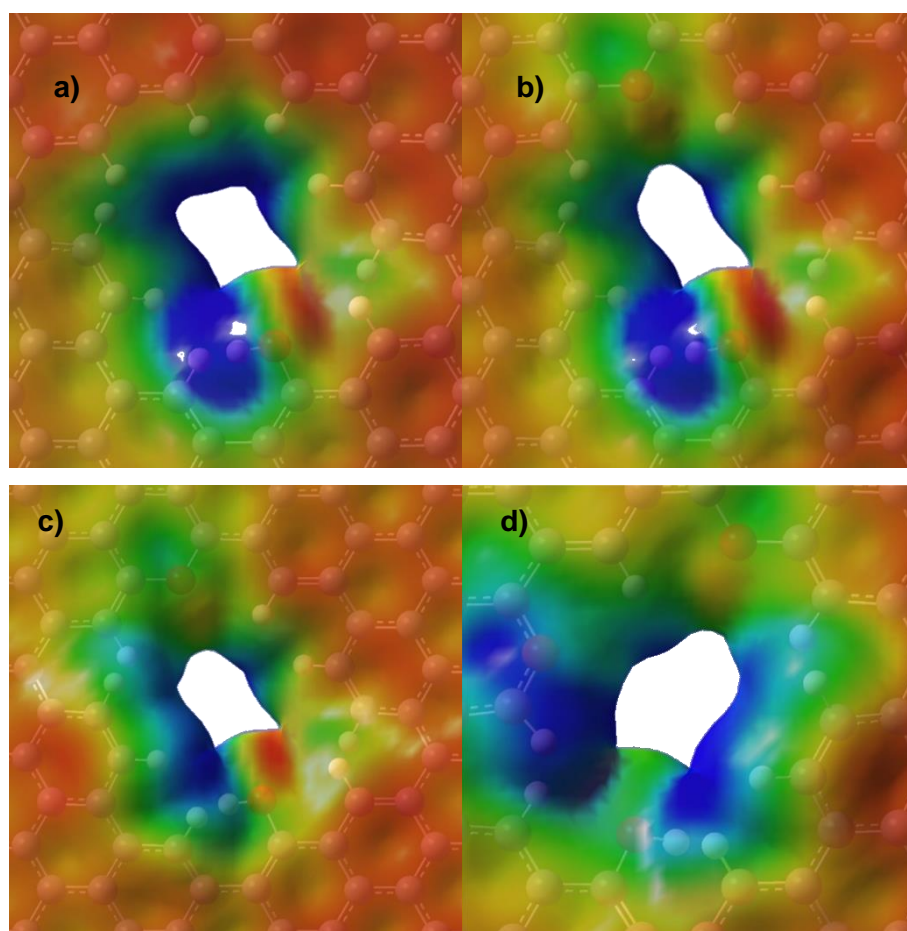
Figure 23 – Close-up of the electrostatic potential maps of a) Vallejos-A hole; b) Vallejos-B open conformation; c) Vallejos-B close conformation and d) Vallejos-C hole.

From the analysis of the latter figures it is possible to see that the size of the different nanowindows in the membrane is increasing with the addition of the ether group, due to the removal of a hydrogen atom and the difference in the electronegativity of the oxygen when compared with the carbon. It is also possible to compare the different size and shape of the pocket in the different conformations of Vallejos-B holes (**Figure 23**). As expected, the open conformation for the Vallejos-B hole has a larger size than the closed one, due to the position of the hydrogen in the nanowindow (**Figure 23- b)** and **c)**).

Another important comparison to make in this study, is the influence of the nanowindow in the shape of the pocket where it will occur permeation. In **Figure 24** it is possible to see the side-view (better to demonstrate the pocket shape) of the different membranes created for this study.
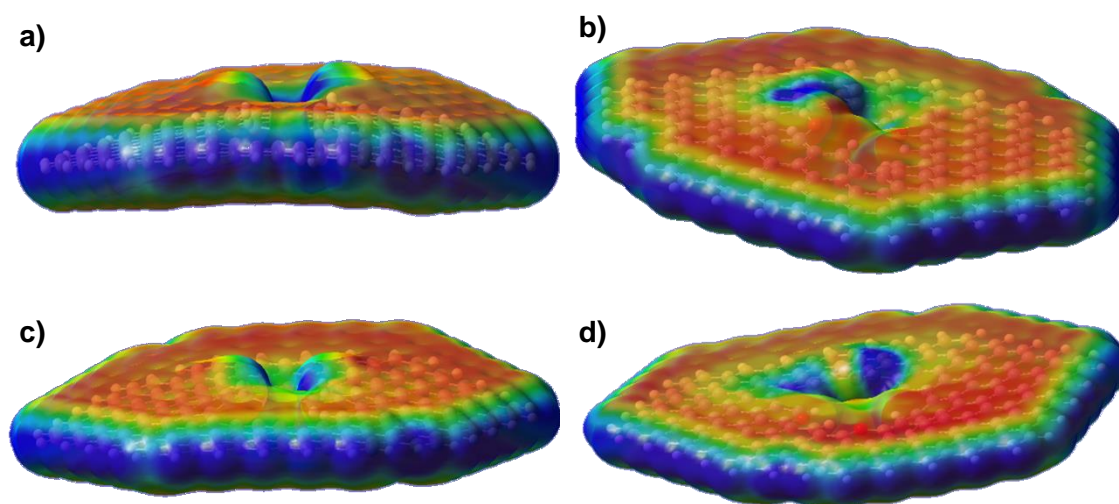
Figure 24 – Side-view of the electrostatic potential maps of a) Vallejos-A hole; b) Vallejos-B open conformation; c) Vallejos-B close conformation and d) Vallejos-C hole.

With the observation of the different pockets in the different membranes that are present in **Figure 24**, we can observe that the pockets tend to be linear with the exception of the Vallejos-B open conformation (**Figure 24- b)**). This pocket is tilted to an oblique side and as referred before, it is bigger than the Vallejos-B closed conformation and this can be justified by a direct consequence of the orientation of the opposing hydrogens duplets are in space. The permeating molecules can assume a linear trajectory due to the fact that the duplets are on the same side of the membrane for Vallejos-A and Vallejos-B close conformation and due to the addition of the ether group rigidness, on Vallejos-C hole.

In order to compare the sizes between these holes, where the atoms are freely to optimize, and the rigid state, the same study was performed for the membrane using the *foutnoh* optimization state. Similarly, in **Figure 25** is displayed an example of the results obtained for this study.
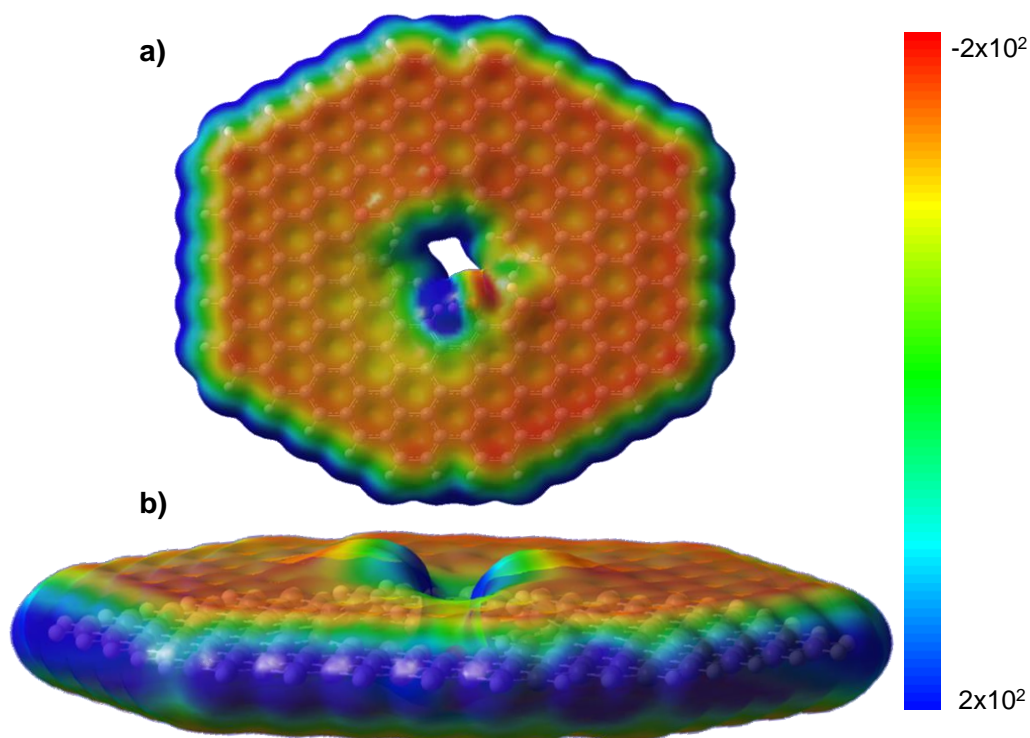
Figure 25 – Electrostatic potential maps of rigid Vallejos-A hole; a) front-view and b) side-view.

The nanowindow-rim chemistry is very similar between both cases, and it is possible to see that the sizes obtained for the membranes are very similar between both states, however when using the rigid approach the pocket size becomes smaller, *e.g.*, **Figure 26** shows this effect for Vallejos-B open conformation. This result was expected due to the restrictions that the systems have in their geometry, as it is possible to see by the linear shape of the membrane in **Figure 25**- **b)**.
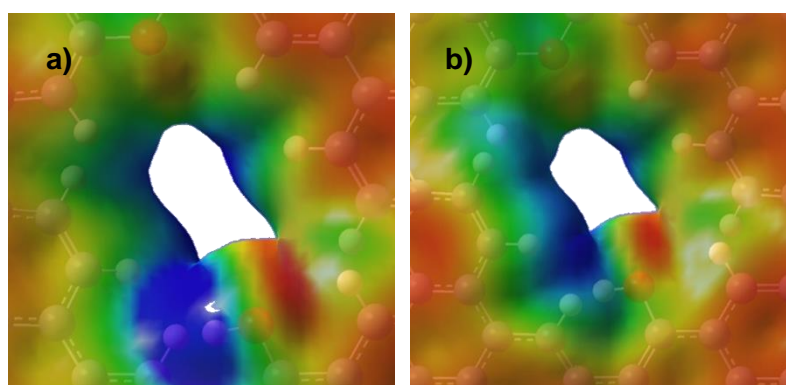
**Figure 26 – Close-view of the electrostatic potential maps of Vallejos-B open conformation;
in which a) flexible membrane and b) rigid membrane.**

In order to be easier to compare both optimization states and size of the different pockets, a comparison between the sizes of both states was performed. For this analysis two different procedures were considered. For the first case, a geometric approach was considered, in which the smaller distance observed in the nanowindow between points of the electron density maps, was calculated. For this, a sphere was designed in the middle of the pocket and afterwards it was compared with a known distance, as it is demonstrated in **Figure 27**. This geometric methodology is similar with the work performed by Vallejos [5], that fitted an identical sphere inside the pocket. However, instead of using the electrostatic potential map, they used the VdW size of all atoms to shape the membrane and the pocket size.
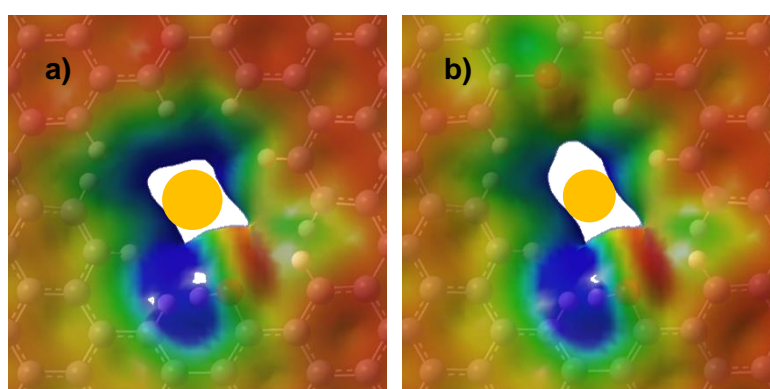
Figure 27 – Geometric approach for the calculation of the diameter of the pocket in a) Vallejos-A hole and b) Vallejos-B open conformation.

The second approach took into consideration a mathematical method. For this the smaller distance observed between atoms in opposite sides of the membrane was calculated. With this data, an analysis of the electron density in a straight segment ($\overline{AB}$) that contain both atoms was performed (**Figure 28- a)**) and the resulting graph was observed (**Figure 28- b)**).
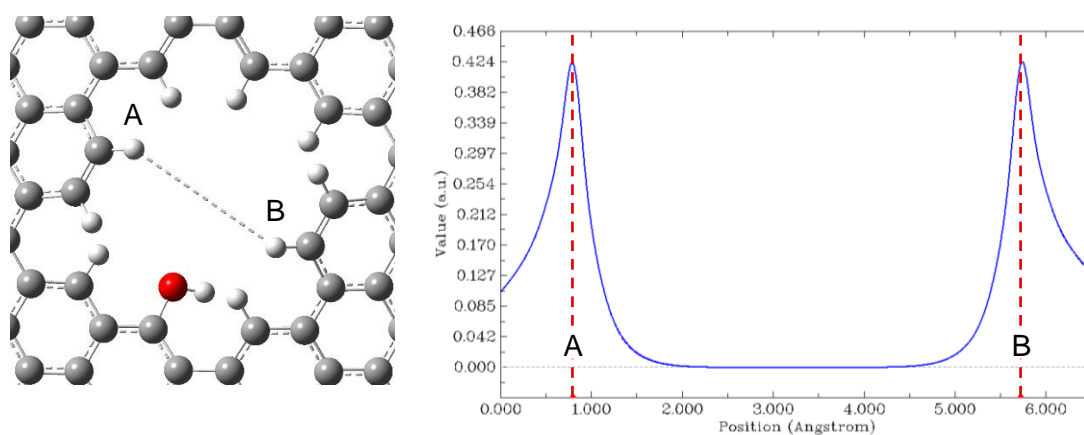
Figure 28 – Mathematical method for the calculation of the diameter of the pocket in Vallejos-A hole; a) minimal distance between atoms and b) electron density vs relative position in the $\overline{AB}$ segment - graph.

As it is possible to see from the **Figure 28- a)**, the electron density approaches zero when there are no atoms, therefore it is possible to determine the size of the nanowindow pocket. For this determination the calculation of the gradient was performed and all the points below 1 % of the maximum value (they exhibit small variation) are accounted and with the limiting cases, we achieved the atomic size of the pocket in the membrane.

These methodologies were applied to all membranes and in the next table, it is possible to compare the size of the different pockets in study using different approximations with the literature (**Table 9**).

Table 9 – Comparison between the size (in Å) of the different pockets in study with literature and the method that we used for its calculation; the first line of each hole refers to the flexible membrane and the second for the rigid membrane.

	Ref. [5]	Geometric method	Mathematical method
Vallejos-A	2.57	2.085	2.706
		1.564	2.680
Vallejos-B open	2.73	1.598	3.012
		1.911	2.981
Vallejos-B closed		1.737	2.873
		1.651	2.829
Vallejos-C	2.97	2.346	3.127
		2.085	3.062

The geometric methodology demonstrated smaller sizes than expected, however it is possible to explain these results, since the measurement is performed in the plane of the membrane, neglecting the fact that the pocket aperture is actually bigger as it is leaning to an oblique side. Even though this approach is the more similar to the applied in Vallejos work, it took into consideration the electrostatic map. Thus, the actual size of the membrane is different than the VdW radii. A comparation between the results will not be performed, and this approach will only be use as a qualitative analysis of the pocket size, therefore it is possible to observe from the data in **Table 9** that the flexible membrane has always larger pocket sizes than the rigid.

Taken into consideration the mathematical approach, the obtained results are much closer than those found in the literature. This methodology follows a deviation index (1 % of the gradient) and results in a more correct approach to the determination of the pocket sizes. Similarly to geometric approach, it is possible to observe that the pocket size increases with higher degrees of freedom that the outer atoms in the membrane have, therefore we can conclude that for this work the flexible membrane approximates our system to the ideal.

After this point the rigid membrane is possible to be discarded for the next study we are performing due to the time required for the full study, as well as the data found in **Table 8** and **Table 9**.

4. Permeation studies

As referred in the introduction, the aim of this work is the study of the efficiency of graphene membranes in the permeation of air and ions in solution. Membrane-based technologies have the potential to completely change separation processes if they ever become efficient. In order to fully comprehend the process of permeation through a membrane, we choose to start by performing the analysis of the permeation of gases in vacuum.

4.1 Permeating air molecules

The separation of the main air components is a process that usually is performed using air separation units (ASU), in which it is possible to obtain oxygen, nitrogen, argon and other rare gases through a combination of high energy demanding processes, such as cryogenic distillation and the compression of large volumes of air [2, 149]. Therefore, we choose to use these gases (N_2, O_2 and Ar) for the permeation studies.

The preview of the permeation is possible to be performed by the analysis of the effective sizes of the air molecules in study. The sizes of molecules in confined spaces depend greatly on the orientation that the molecule can adopt inside the restricted space, such as the nanowindows in study. Therefore, the VdW molecular diameter should not be used has a consistent size for this study. Through the years, a more rigorously defined kinetic diameter started to be used, in which the intermolecular distance of the closest approach of two molecules of zero kinetic energy [150, 151]. However, it still fails due to the inadequacy of a single molecular dimension. Since the critical molecular dimension is dependent on the pore shape, it is important to check the smallest dimension that the molecule can achieve (MIN-1) and the intermediate dimension (MIN-2), which is related to the largest constrained dimension that the molecule can achieve. The latter dimension, *i.e.* MIN-2, relates better to a cylindrical pore [5, 151-153]. In **Table 10**, it is possible to find the dimensions of the molecules that are taken into consideration for our study [151].

Table 10 – Dimensions of the air molecules for this study.

	Kinetic diameter / nm	MIN-2 dimension / nm
N_2	0.36	0.31
O_2	0.35	0.30
Ar	0.34	0.36

A good membrane should have a nanowindow size that ranges near the limits close to the dimensions that are present in **Table 10**, in order to achieve some selectivity for the separation of the air components. As it is possible to check from the data in **Table 9**, the nanowindows created are in agreement with this statement. In literature it is also documented that these membranes showed great promise to the separation of air main constituents [5].

The air molecules that were used in this study, also have very different type of interactions which is important for the information it provides about their interactions with the nanowindow-rim. As it is known, Argon is an element that is from the eighteen group from the periodic table, it is a noble gas, therefore it interacts very weakly with the functional groups that are present in the nanowindow-rim. However, N_2 and O_2 possess two quadrupole moments that can interact through electrostatic interactions due to the atoms present at the different nanowindows created. Thus, it is possible with these main air components to have a study of a selective separation of different molecules with similar sizes but with different types of molecular interactions, such as dispersive or electrostatic. For instance it has already been demonstrated and studied that N_2 adsorbs greatly in graphene membranes [154].

4.1.1 Methodology applied

The study of the permeation of the main air constituents utilizing QM can be performed with the Gaussian software by using different approaches. For this study, we tested the scan method and the point by point optimization steps.

The scan keyword makes a relaxed potential energy surface (PES) scan, in which it is possible to get different optimizations at each point of the intended variation. Typically, this method works great in systems that require a small number of atoms, a low-performance functional and a lower basis set, however when you try to scale it for our system some errors may occur. Another factor that makes this method difficult to apply is that we are moving an atom (*e.g.* Ar) or a molecule (*e.g.* N_2 or O_2) from one position to another using step-by-step approach of a bond length defined with a dummy or a ghost atom. The usage of dummies in optimization processes are impossible to be performed, therefore only Ghost atoms could be used. The intended M06-2X functional and 6-31G(d) basis set were tried for this study, however it outputted several errors, such as RedCar and no convergence for the initial points, even when the starting point was already optimized before. In order to try to make this method work, even different

attempts were performed, such as using the B3LYP functional with lower basis set (6-31G), the usage of different convergence criteria and even using different optimization algorithms, however this methodology never permitted the study to continue, therefore it was eventually discarded and the step-by-step approach was taken into consideration. With the latter it is possible to perform the full study with different calculations of an approaching atom or molecule, however it requires a lot more computational time due to the number of optimizations that are required to be made.

4.1.2 Linear step-by-step approach

In order to fully study the permeation of an atom or molecule through our membranes, an initial approximation was performed. The molecule that was permeating was approaching the system in study, linearly at a perpendicular angle, as it can be observed in **Figure 29**.
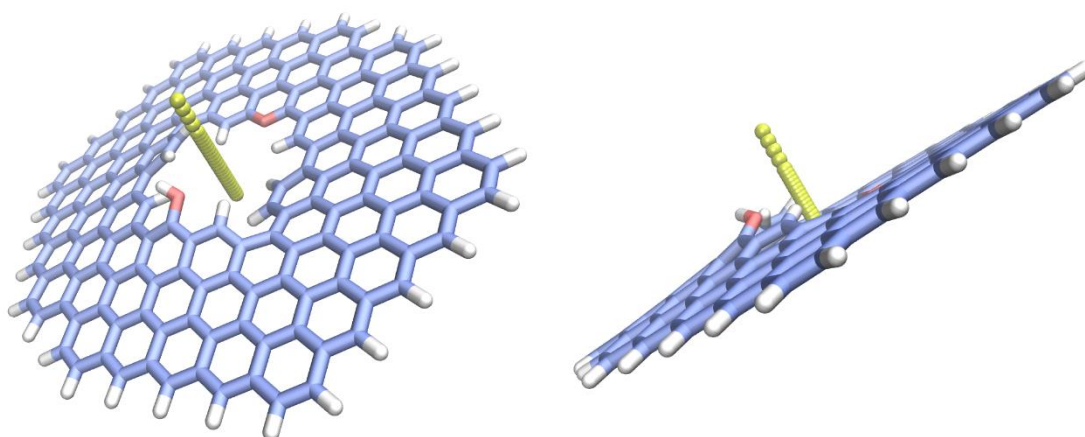
Figure 29 – Demonstration of the linear step-by-step approximation of Ar to the membrane (the image was created using VMD software [155]).

We choose to start with the study of the permeation of Argon through our membranes due to it only being a single atom, which simplifies the input and calculations required. The absence of interactions with the membrane are also another important factor for this choice, because it will not adsorb to the graphene membrane when it gets far away from the nanowindow, simplifying greatly the optimizations.

For this study, the Ar atom was putted at the centre of the nanowindow and it was added sequentially different distances to the membrane (altering the Z-coordinate). Afterwards, several optimizations were performed with the Ar position changing 0.2 Å between each step. With the results obtained by this approach, it was possible to make a plot of the energetic difference vs distance to the centre of the nanowindow

(**Figure 30-32**). The energetic difference was calculated following the next equation, in which the values obtained for the different optimizations were subtracted with the values obtained for the infinite distance possible between Ar and the membrane, *i.e.*, the optimization for Ar and the membrane was performed in different files.

$$\Delta E = E_{graphene/Ar} - (E_{graphene} + E_{Ar})$$

Equation 52 – Clarification of the calculation of the energetic difference for the plot observed in Figure 30-32.

The linear study of the permeation of the Ar atom was performed for the Vallejos-B open (**Figure 30**) and closed (**Figure 31**) conformation, as well as the Vallejos-C hole (**Figure 32**). Even though the rigid membrane could be discarded, it was also taken into consideration the different optimization states possible, in order to obtain an idea of the results that could be obtained by letting the membrane freely optimize or by imposing restrictions on the system.

Figure 30 – Graph of the energetic difference vs distance of the Ar atom to the centre of the Vallejos-B open conformation nanowindow

With the analysis of this graph it is possible to see that there are small energetic variations observed in the flexible membrane at 1.8 and -1.2 Å and in the rigid membrane at 0.4 Å. The peaks of energy associated to the *nof* state are related to the linear approximation that was performed in this study, due to the position of the hydrogen duplets (highlighted by the green bars in **Figure 19**). Since they are located at these positions, it is possible to observe some steric repulsion between the Ar atom and the duplets on each side, which increases the overall energy of the system. The 0.4 Å peak located in the *foutnoh* state appears due to the position of the hydroxyl group (highlighted by the red arrows in the latter figure), which leads to a smaller size of the pocket, as demonstrated in **Table 9**, therefore the repulsion is higher between Ar and the membrane inside the pocket.

Figure 31 – Graph of the energetic difference vs distance of the Ar atom to the centre of the Vallejos-B closed conformation nanowindow

The latter graphic demonstrates again the steric repulsion observed at 1.6 Å, as it is possible to see the peak in the energetic difference in both states. The energetic difference between the peak observed in **Figure 30** and **Figure 31** are related with the fact that the Vallejos-B hole contain the duplets pointing to the same side, which makes the pocket way smaller and harder to permeate. Even though with these results it is already possible to say that the linear approximation is not the best approach for the permeation studies due to the increase in energy when the permeating molecule is near the hydrogens, it was possible to check that it is harder to permeate the Vallejos-B closed conformation than the open due to the energetic difference observed between peaks.

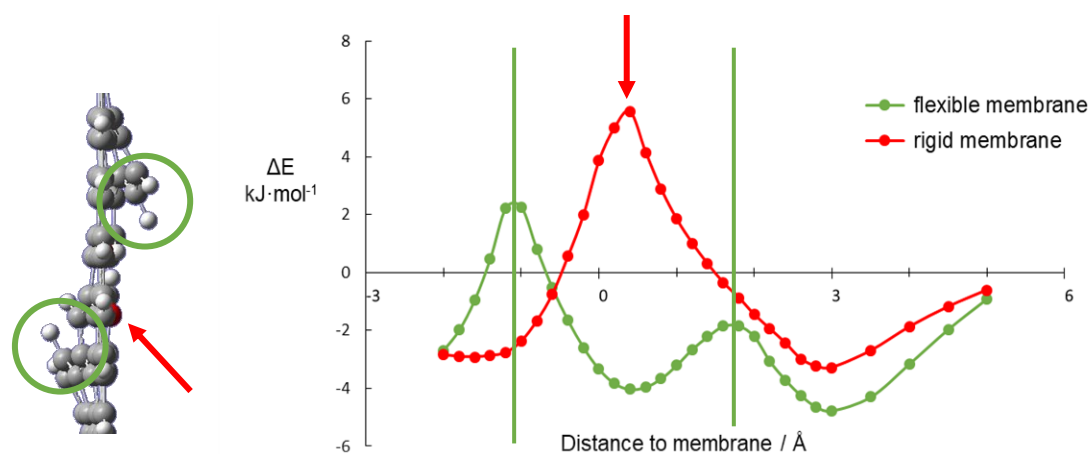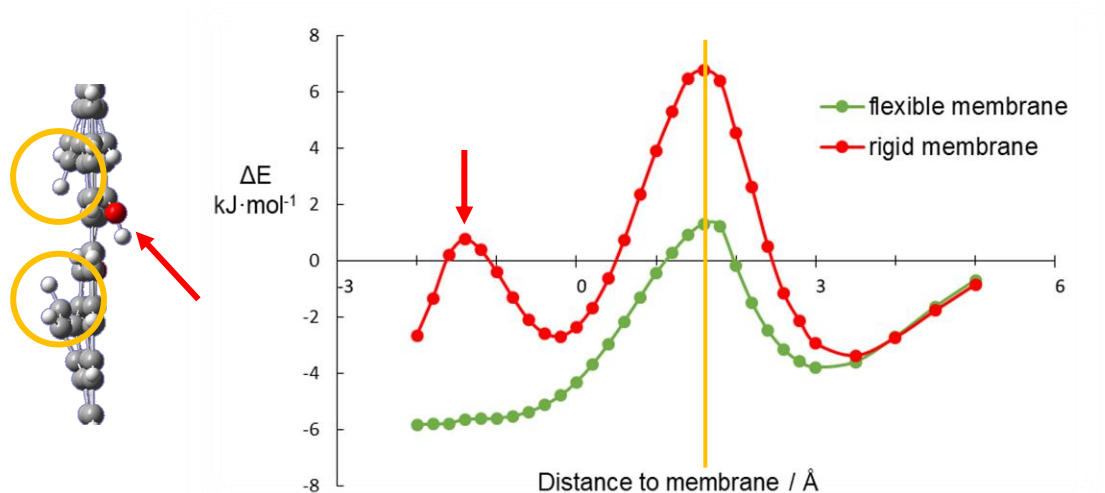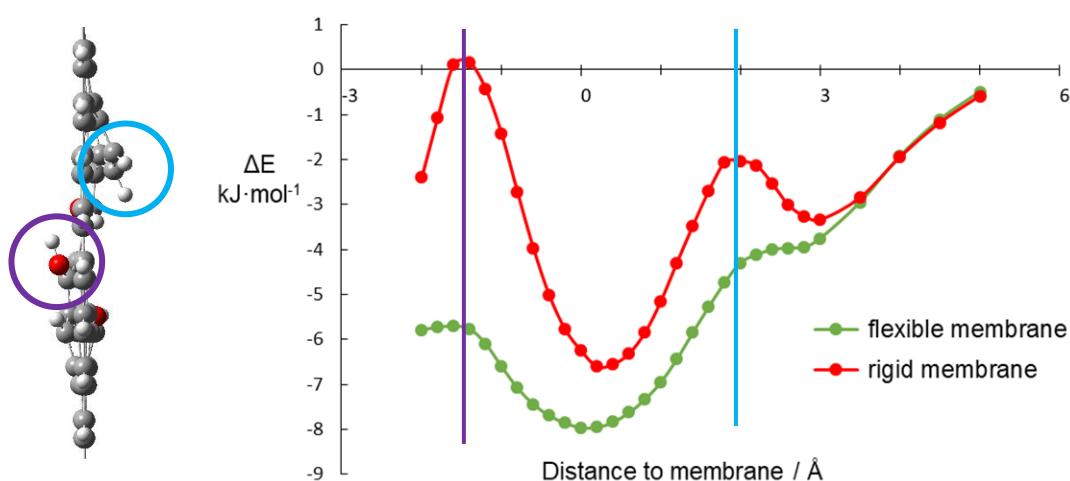**Figure 32 – Graph of the energetic difference vs distance of the Ar atom to the centre of the Vallejos-C nanowindow.**

As it is possible to observe from the latter graphic, at the centre of the membrane the energy is low therefore permeation through the Vallejos-C hole can occur, however there is still some repulsion observed at 2.8 and -1.5 Å, due to the position of the duplets, highlighted at blue; and the hydroxyl group, highlighted at purple in **Figure 32**, which can difficult the permeation through this hole. This study only takes into consideration certain points in the geometry and not the full pathway, as normally observed in MD simulations studies. It is surprising that Ar can permeate, even when performing this linear approximation since its effective size (3.63 Å), is larger the diameter of the pore (3.127 Å), as mentioned before in **Table 10** and **Table 9**, respectively.

The study of the permeation through the Vallejos-A hole membrane was not performed since the work in the literature [5], using MD, demonstrated that there is no permeation observed in this hole of the membrane. In that work, Vallejos-Burgos *et al.*, demonstrated that permeation was only possible for the O_2 molecule through the Vallejos-B hole and that all molecules in study could permeate through higher holes sizes than Vallejos-C hole. The next figure is adapted from his work and shows the permeation rate of the permeating molecules in study for Vallejos-A, -B, and -C holes.
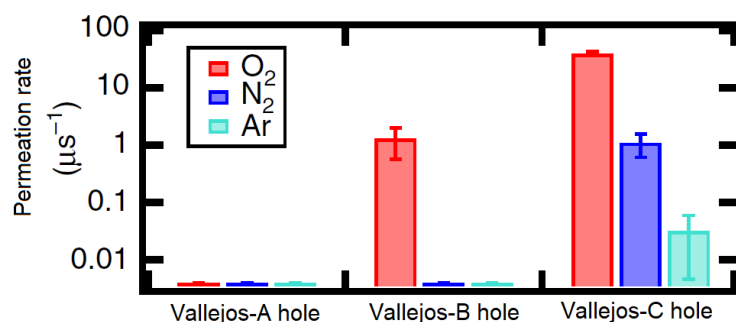
Figure 33 – Permeation rate through the different membranes in study, adapted from [5].

The analysis of the latter figure leads to the confirmation that Vallejos-C can be permeated by Ar, however in order to be more certain about our study a new approach is required for to be done. Vallejos-B hole also shows selectivity towards the O_2/N_2 separation, in a relative high ratio (~20:1) [67].

4.1.3 Free step-by-step approach

It has been shown that almost all gases that is trying to permeate through a graphene nanowindow, has normally two local minima. Normally, small molecules of gases tend to be adsorbed on the basal plane at a distance of *ca.* 3.3 Å of the basal plane and when the interaction between the nanowindow and the pore begin, therefore

a linear approach neglects these different stages of the permeation mechanism [5, 107, 156, 157]. With that in mind, several attempts were performed in order to make a functional calculation procedure that can take into consideration this type of mechanism.

The molecule that is permeating can freely approach the system in study, as it can be observed in **Figure 34**.
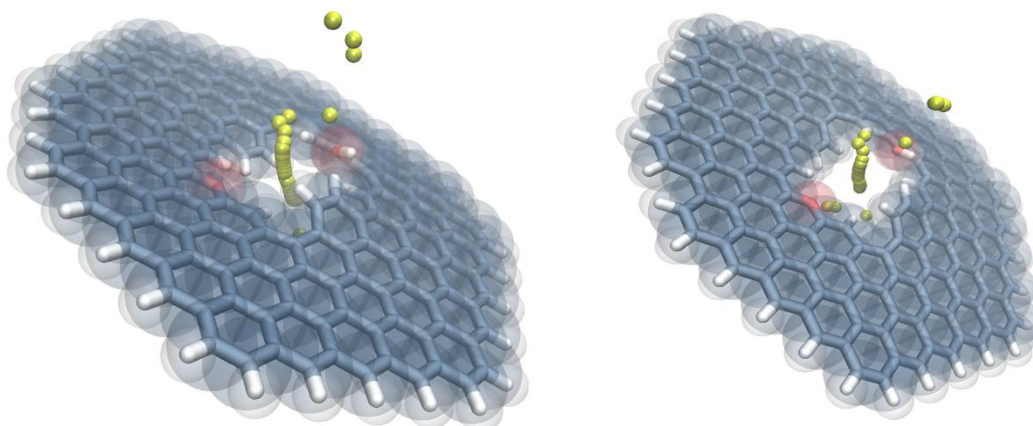
Figure 34 – Demonstration of the free step-by-step approximation of Ar to the membrane (the image was created using VMD software)

This study was performed for the permeation of Ar atom, and O_2 and N_2 molecules, for the three different membranes that were debated above, the Vallejos-B open conformation and closed and to Vallejos-C.

The results obtained for Ar can be found in the next figure. It is important to note the pathway that Ar follows in order to pass by the hole, in order to understand the energy observe due to the interactions that can be established (**Figure 34**, shows the pathway that it follows in the Vallejos-B open hole and it is very similar with the other two).

Figure 35 – Graph of the energetic difference vs distance of the Ar atom to the centre of the Vallejos-B open and closed; and Vallejos-C nanowindow.

When the Ar atom is free to approach the graphene nanowindow, it is possible to see that the energies are as an overall lower. It is possible to see from the blue dots, associated with the Vallejos-B open conformation, that the permeation is possible to occur, however there is a small increase in energy in the centre of the membrane when the Ar atom squeezes through the nanowindow rim, as the hydroxyl that is in the aligned with the basal plane, has repulsive interactions with the permeating atom. Taking into consideration the Vallejos-B closed conformation, in orange, it is possible to see the big increase in energy where the double hydrogen doublets are located. This conformation leads to a complete shut-down of the permeation of any molecule, due to this feature. As for the last case, in green, it is possible to confirm the data from **Figure 33** obtained by Vallejos-Burgos, in which there is almost no opposition to the permeation of Ar, even though the atom has superior size than the pore.

The same approach was performed for the permeation of the O_2 and N_2 molecule for the Vallejos-B open (**Figure 36**) and Vallejos-C (**Figure 37**). Vallejos-B closed conformation was discarded because of the data in the latter figure, in which there is the complete shut-down of permeation through this nanowindow. The study for Vallejos-C hole in both permeating molecules has a low amount of points due to failures in convergence and in positioning, *i.e.* gave rise to some RedCar error, that normally occurs when the molecule is adsorbed into the graphene wall.
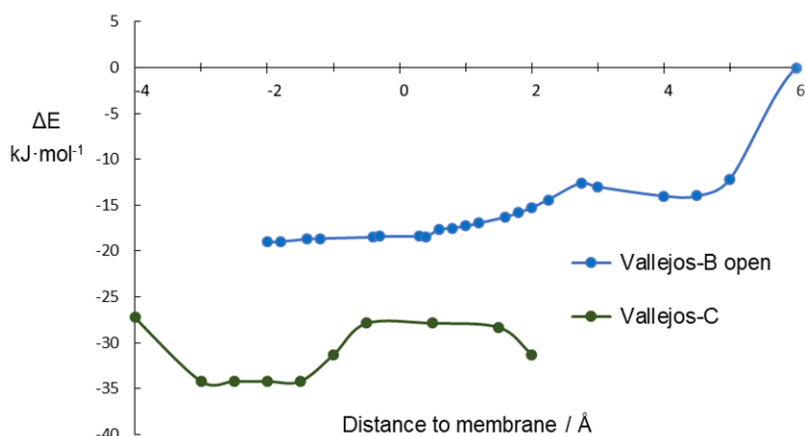
Figure 36 – Graph of the energetic difference vs distance of the O$_2$ atom to the centre of the Vallejos-B open and Vallejos-C nanowindow.

From the direct analysis of the **Figure 36**, it is possible to see that both Vallejos-B open and Vallejos-C nanowindows, allow the permeation of O$_2$. This follows the permeation rate demonstrated in **Figure 33**, and the information present in both **Table 9** and **Table 10**. O$_2$ can permeate freely through these nanowindows due to its smaller size (3.0 Å), lacking repulsion interactions even when they pass through the nanowindow rim. The difference in the pore size facilitates the permeation through the Vallejos-C nanowindow as there is about 10 kJ·mol^{-1} of difference to the Vallejos-B hole.
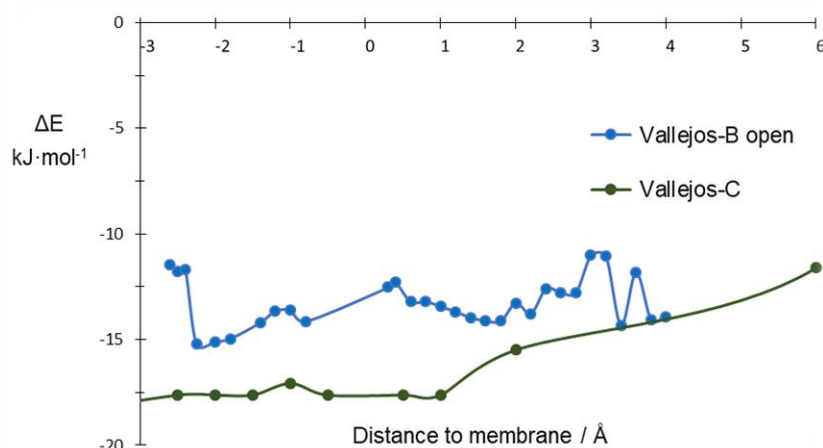
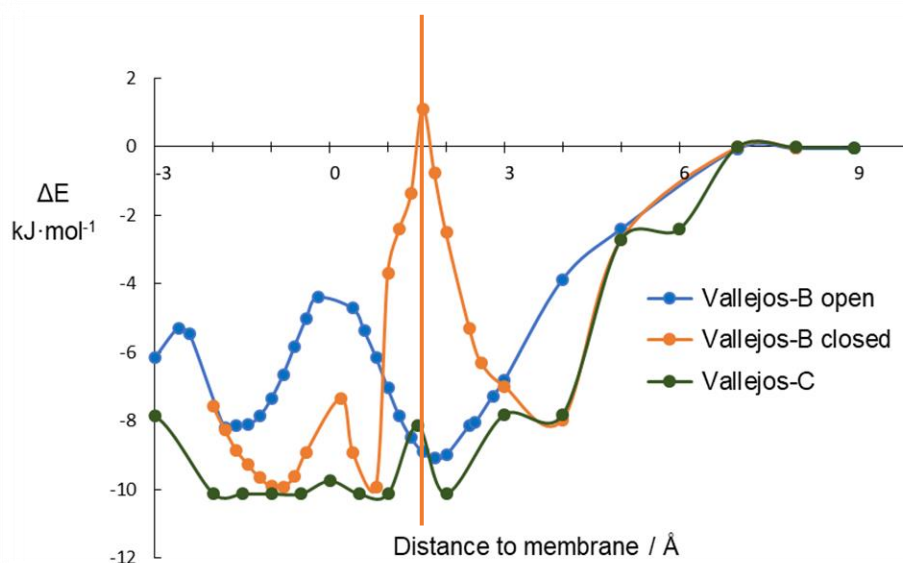**Figure 37 – Graph of the energetic difference vs distance of the N$_2$ atom to the centre of the Vallejos-B open and Vallejos-C nanowindow.**

The passage of N$_2$ through these membranes is fairly easy, as there is no positive contribution or any high energetic variation observed in the latter graphic. However, since the points closer to the centre of the membrane gave rise to some errors, mostly convergence, this analysis can be a bit inconclusive. It is known, from the work of

Vallejos-Burgos, that N_2 has a high repulsive character when it comes to the centre of the membrane, but this increase in energy is counterbalanced by a strong electrostatic stabilization, which leads to a low rate of permeation through the holes (when compared with O_2) [5]. The combination between his work and our results, allows to say that permeation can be observed, however further calculations must be performed.

4.2   Permeation in solution

The study of permeation of ions in solution was initiated by the optimization of the nanowindows referred before, in order to achieve a full characterization of one system. The resulting geometry and the respective results for the Vallejos-B open nanowindow was obtained using an PCM model and can be found in the next figure and table. Both the rigid and the flexible membrane were considered for this initial optimization procedure.

Table 11 – Energetic difference between the different states, using the flexible membrane as the reference and comparation with the results obtained in vaccum.

|	Vallejos-B$_{open}$ / vaccum	Vallejos-B$_{open}$ / solution
$\Delta E_{nof \rightarrow foutnoh}$ / kJ·mol^{-1}	317.7	321.0
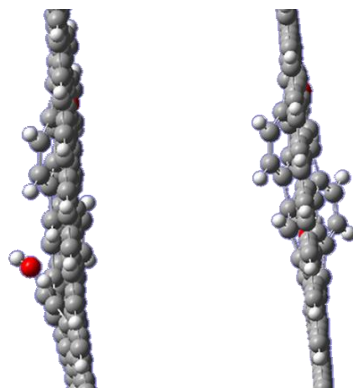
Figure 38 – Graph of the energetic difference vs distance of the N_2 atom to the centre of the Vallejos-B open and Vallejos-C nanowindow.

The difference observed between the optimization of both the rigid and the flexible approach in water and in vacuum is almost negligible (**Table 11**), however the flexible membrane in water assumes more curvature than the observed normally in vacuum (**Figure 38**). The comparison between the open and closed conformation of Vallejos-B hole using water as a solvent was also performed and it can be observed in **Table 12**.

Table 12 – Comparison between the energetic difference observed in the different conformations of Vallejos-B hole with the literature, in vacuum and solution.

	Ref. [5] vaccum	Flexible membrane vaccum	Flexible membrane water solution
$\Delta E_{conformations}$ kJ·mol^{-1}	1.3	1.99	2.86

It is possible to see that there is a smaller deviation on the energetic difference between the open and closed conformations when we introduced water as a solvent. This goes according to what is expected, since the molecules in solution can stabilize the membrane reducing more their energy.

The study of the permeation of ions in solution did not go past this point, due to the time that was required to perform the vacuum part, however these initial properties studied prove to be appealing for further calculation.

E. CONCLUSIONS AND FUTURE PERSPECTIVES

"*In literature and in life we ultimately pursue, not conclusions, but beginnings*".

Sam Tanenhaus

The world is in dire need of solutions towards all the resulting chaos that comes from the carbon dioxide emissions. Ironically enough, one way to contest these problems is the usage of a carbon-based material as a solution towards the reduction of these emissions in the separation procedures that require phase change transitions.

In the present work, we demonstrate that the main constituents of air can permeate selectively through certain graphene nanowindows. We were able to perform the study of the permeation of air molecules through different nanowindows present in graphene and start to pave the way into the study of those nanowindows for the permeation of ions in solution. A full characterization and parametrization of further studies was performed in vacuum, which can allow the application of different membranes to the study presented in this work. This is an important aspect of this work, due to the fact that this procedure took some time to be accomplished. The permeation studies are also a bit time consuming due to the several separated files that are needed to compute, however the calculations are now fully optimized to reduce the computational time required. Consequently, the study of the permeation of ions in solution has been delayed and it needs to be further explored in a future work.

We were able to conclude that the energetic difference between the Vallejos-B open and closed conformations, obtained in a MD related study (1.3 kJ·mol^{-1}), was in fact bigger if we take into consideration a DFT procedure (1.99 kJ·mol^{-1}). It was also confirmed that the permeation through the closed conformation was not possible to occur. For pocket apertures bigger than the Vallejos-C hole (3.127 Å) can be the starting point for every air molecule to permeate, although they would not have any selectivity.

The research around carbon nanomaterials for the permeation of air and ions in solution is essential, as they have been proven to be good to perform the separation of these compounds in several MD simulation studies. The accurate description of the nanowindow rim-chemistry is one of the main advantages of our approach and should be performed for bigger membranes and with different functionalization. The permeation

study of molecules using DFT is a bit hard to perform, however they provide a better understanding of the interactions in the pocket site. Therefore, extending these studies to CH_4 and CO_2 could prove to have added value, since they compose a part of our atmosphere and can serve as a template for bigger compounds, *e.g.*, if CH_4 cannot permeate through a certain membrane, it is possible to say that no hydrocarbon can pass through the nanowindow.

Although there are some missing points and some issues to resolve within our approach, the information contained in this work can be used for the comprehension of the permeation of both air in vacuum and ions in solution through graphene nanowindows, as these are either in agreement or even upgrade some of the results present in the literature.

F. REFERENCES

1. Freemantle, M., Membranes for gas separation. *Chemical & Engineering News Archive* **2005,** *83* (40), 49-57.

2. Tsay, C.; Baldea, M.; Shi, J.; Kumar, A.; Flores-Cerrillo, J., Data-Driven Models and Algorithms for Demand Response Scheduling of Air Separation Units. In *Computer Aided Chemical Engineering*, Eden, M. R.; Ierapetritou, M. G.; Towler, G. P., Eds. Elsevier: 2018; Vol. 44, pp 1273-1278.

3. Dutcher, B.; Fan, M.; Russell, A. G., Amine-Based CO2 Capture Technology Development from the Beginning of 2013—A Review. *ACS Applied Materials & Interfaces* **2015,** *7* (4), 2137-2148.

4. Sholl, D. S.; Lively, R. P., Seven chemical separations to change the world. *Nature* **2016,** *532* (7600), 435-437.

5. Vallejos-Burgos, F.; Coudert, F.-X.; Kaneko, K., Air separation with graphene mediated by nanowindow-rim concerted motion. *Nature Communications* **2018,** *9* (1), 1812.

6. Qu, X.; Alvarez, P. J. J.; Li, Q., Applications of nanotechnology in water and wastewater treatment. *Water Research* **2013,** *47* (12), 3931-3946.

7. Surwade, S. P.; Smirnov, S. N.; Vlassiouk, I. V.; Unocic, R. R.; Veith, G. M.; Dai, S.; Mahurin, S. M., Water desalination using nanoporous single-layer graphene. *Nature Nanotechnology* **2015,** *10*, 459.

8. Oberhummer, H.; Csótó, A.; Schlattl, H., Stellar Production Rates of Carbon and Its Abundance in the Universe. *Science* **2000,** *289* (5476), 88.

9. Bailey, C. H., The Origin of Life (Oparin, A. I.). *Journal of Chemical Education* **1938,** *15* (8), 399.

10. Mathur, R. B.; Singh, B. P.; Pande, S., *Carbon Nanomaterials Synthesis, Structure, Properties and Applications*. 2017.

11. Maksić, Z. B., Symmetry, hybridization and bonding in molecules. *Computers & Mathematics with Applications* **1986,** *12* (3, Part 2), 697-723.

12. Alabugin, I. V.; Bresch, S.; dos Passos Gomes, G., Orbital hybridization: a key electronic factor in control of structure and reactivity. *Journal of Physical Organic Chemistry* **2015,** *28* (2), 147-162.

13. Bundy, F. P.; Bassett, W. A.; Weathers, M. S.; Hemley, R. J.; Mao, H. U.; Goncharov, A. F., The pressure-temperature phase and transformation diagram for carbon; updated through 1994. *Carbon* **1996,** *34* (2), 141-153.

14. Fuchs, J.-N.; Goerbig, M. O., Introduction to the physical properties of graphene. 2008.

15. Dresselhaus, M. S., Future Directions in Carbon Science. *Annual Review of Materials Science* **1997,** *27* (1), 1-34.

16. Field, J. E., The mechanical and strength properties of diamond. *Reports on progress in physics. Physical Society (Great Britain)* **2012,** *75* (12), 126505.

17. Kroto, H. W.; Heath, J. R.; O'Brien, S. C.; Curl, R. F.; Smalley, R. E., C60: Buckminsterfullerene. *Nature* **1985,** *318* (6042), 162-163.

18. Iijima, S., Helical microtubules of graphitic carbon. *Nature* **1991,** *354* (6348), 56-58.

19. Novoselov, K. S.; Geim, A. K.; Morozov, S. V.; Jiang, D.; Zhang, Y.; Dubonos, S. V.; Grigorieva, I. V.; Firsov, A. A., Electric Field Effect in Atomically Thin Carbon Films. *Science* **2004,** *306* (5696), 666.

20. Dresselhaus, M. S.; Dresselhaus, G.; Eklund, P. C., Science of Fullerenes and Carbon Nanotubes : Their Properties and Applications. **1996**.

21. NobelPrize.org The Nobel Prize in Chemistry 1996. https://www.nobelprize.org/prizes/chemistry/1996/summary/ (accessed Wed. 9 Jul 2019).

22. Marsh, H., *Introduction to carbon technologies.* University of Alicante, Secretariado de Publicaciones: Alicante, Spain, 1997.

23. Hurt, R., Chemistry and Physics of Carbon. Volume 27 Edited by Ljubisa R. Radovic. *Journal of the American Chemical Society* **2001,** *123* (41), 10141-10141.

24. Kumar, M.; Raza, K., C60-fullerenes as Drug Delivery Carriers for Anticancer Agents: Promises and Hurdles. *Pharmaceutical nanotechnology* **2017,** *5* (3), 169-179.

25. Schwerdtfeger, P.; Wirz, L. N.; Avery, J., The topology of fullerenes. *Wiley Interdiscip Rev Comput Mol Sci* **2015,** *5* (1), 96-145.

26. Francis, A. H., An Atlas of Fullerenes By P. W. Fowler, D. E. Manolopoulos. *Journal of the American Chemical Society* **1996,** *118* (21), 5161-5161.

27. Prato, M., [60]Fullerene chemistry for materials science applications. *Journal of Materials Chemistry* **1997,** *7* (7), 1097-1109.

28. Manolopoulos, D. E.; May, J. C.; Down, S. E., Theoretical studies of the fullerenes: C34 to C70. *Chemical Physics Letters* **1991,** *181* (2), 105-111.

29. Haddon, R. C.; Brus, L. E.; Raghavachari, K., Electronic structure and bonding in icosahedral C60. *Chemical Physics Letters* **1986,** *125* (5), 459-464.

30. Diederich, F.; Thilgen, C., Covalent Fullerene Chemistry. *Science* **1996,** *271* (5247), 317.

31. Fowler, P. W.; Manolopoulos, D. E., Magic numbers and stable structures for fullerenes, fullerides and fullerenium ions. *Nature* **1992,** *355* (6359), 428-430.

32. Albertazzi, E.; Domene, C.; W. Fowler, P.; Heine, T.; Seifert, G.; Van Alsenoy, C.; Zerbetto, F., Pentagon adjacency as a determinant of fullerene stability. *Physical Chemistry Chemical Physics* **1999,** *1* (12), 2913-2918.

33. Ruoff, R. S.; Ruoff, A. L., The bulk modulus of C60 molecules and crystals: A molecular mechanics approach. *Applied Physics Letters* **1991,** *59* (13), 1553-1555.

34. Wilson, M. A.; Pang, L. S. K.; Willett, G. D.; Fisher, K. J.; Dance, I. G., Fullerenes—preparation, properties, and carbon chemistry. *Carbon* **1992,** *30* (4), 675-693.

35. Di Ventra, M.; Evoy, S.; Heflin, J. R., *Introduction to nanoscale science and technology*. Kluwer Academic Publishers: Boston, 2004.

36. Montellano López, A.; Mateo-Alonso, A.; Prato, M., Materials chemistry of fullerene C60 derivatives. *Journal of Materials Chemistry* **2011,** *21* (5), 1305-1318.

37. Dunsch, L.; Yang, S., The recent state of endohedral fullerene research. *Electrochemical Society Interface* **2006,** *15*, 34-38.

38. Polotskaya, G. A.; Penkova, A. V.; Toikka, A. M., Fullerene-containing polyphenylene oxide membranes for pervaporation. *Desalination* **2006,** *200* (1), 400-402.

39. Rokitskaya, T. I.; Antonenko, Y. N., Fullerenol C60(OH)24 increases ion permeability of lipid membranes in a pH-dependent manner. *Biochimica et Biophysica Acta (BBA) - Biomembranes* **2016,** *1858* (6), 1165-1174.

40. Radushkevich, L. V.; Lukyanovich, V. M., The Structure of Carbon Forming in Thermal Decomposition of Carbon Monoxide on an Iron Catalyst. *Russian Journal of Physical Chemistry,* **1952,** *26*, 88-95.

41. Oberlin, A.; Endo, M.; Koyama, T., Filamentous growth of carbon through benzene decomposition. *Journal of Crystal Growth* **1976,** *32* (3), 335-349.

42. Bethune, D. S.; Kiang, C. H.; de Vries, M. S.; Gorman, G.; Savoy, R.; Vazquez, J.; Beyers, R., Cobalt-catalysed growth of carbon nanotubes with single-atomic-layer walls. *Nature* **1993,** *363* (6430), 605-607.

43. Iijima, S.; Ichihashi, T., Single-shell carbon nanotubes of 1-nm diameter. *Nature* **1993,** *363* (6430), 603-605.

44. Vijayaraghavan, A., Applications of chirality-sorted individual single-wall carbon nanotube devices. *Journal of Materials Chemistry* **2012,** *22* (15), 7083-7087.

45. Shulaker, M. M.; Hills, G.; Patil, N.; Wei, H.; Chen, H.-Y.; Wong, H. S. P.; Mitra, S., Carbon nanotube computer. *Nature* **2013,** *501*, 526.

46. Liu, Z.; Sun, X.; Nakayama-Ratchford, N.; Dai, H., Supramolecular Chemistry on Water-Soluble Carbon Nanotubes for Drug Loading and Delivery. *ACS Nano* **2007,** *1* (1), 50-56.

47. Schäffel, F., Chapter 2 - The Atomic Structure of Graphene and Its Few-layer Counterparts. In *Graphene*, Warner, J. H.; Schäffel, F.; Bachmatiuk, A.; Rümmeli, M. H., Eds. Elsevier: 2013; pp 5-59.

48. Dai, H., Carbon Nanotubes: Synthesis, Integration, and Properties. *Accounts of Chemical Research* **2002,** *35* (12), 1035-1044.

49. Mukhopadhyay, G.; Behera, H., Emerging Two-dimensional Materials: graphene and its other structural analogues. **2013**.

50. Wallace, P. R., The Band Theory of Graphite. *Physical Review* **1947,** *71* (9), 622-634.

51. Ando, T., The electronic properties of graphene and carbon nanotubes. *NPG Asia Materials* **2009,** *1*, 17-21.

52. Dürkop, T.; Kim, B. M.; Fuhrer, M. S., Properties and applications of high-mobility semiconducting nanotubes. *Journal of Physics: Condensed Matter* **2004,** *16* (18), R553-R580.

53. Fathi, D., A Review of Electronic Band Structure of Graphene and Carbon Nanotubes Using Tight Binding. *Journal of Nanotechnology* **2011,** *2011*.

54. Berber, S.; Kwon, Y.-K.; Tománek, D., Unusually High Thermal Conductivity of Carbon Nanotubes. *Physical Review Letters* **2000,** *84* (20), 4613-4616.

55. Wei, B.; Vajtai, R.; M. Ajayan, P., Reliability and Current Carrying Capacity of Carbon Nanotubes. *Applied Physics Letters* **2001,** *79*, 1172-1174.

56. Jorio, A.; Dresselhaus, G.; S Dresselhaus, M., *Carbon Nanotubes: Advanced Topics in the Synthesis, Structure, Properties and Applications*. 2008; Vol. 111.

57. Zhang, W.; Zhang, Z.; Zhang, Y., The application of carbon nanotubes in target drug delivery systems for cancer therapies. *Nanoscale Res Lett* **2011,** *6* (1), 555-555.

58. Kar, S.; Bindal, R. C.; Tewari, P. K., Carbon nanotube membranes for desalination and water purification: Challenges and opportunities. *Nano Today* **2012,** *7* (5), 385-389.

59. Majumder, M.; Chopra, N.; Andrews, R.; Hinds, B. J., Nanoscale hydrodynamics: enhanced flow in carbon nanotubes. *Nature* **2005,** *438* (7064), 44.

60. Hummer, G.; Rasaiah, J. C.; Noworyta, J. P., Water conduction through the hydrophobic channel of a carbon nanotube. *Nature* **2001,** *414* (6860), 188-190.

61. Rashid, M. H.-O.; Ralph, S. F., Carbon Nanotube Membranes: Synthesis, Properties, and Future Filtration Applications. *Nanomaterials (Basel)* **2017,** *7* (5), 99.

62. Corry, B., Designing Carbon Nanotube Membranes for Efficient Water Desalination. *The Journal of Physical Chemistry B* **2008,** *112* (5), 1427-1434.

63. Lee, K. P.; Arnot, T. C.; Mattia, D., A review of reverse osmosis membrane materials for desalination—Development to date and future potential. *Journal of Membrane Science* **2011,** *370* (1), 1-22.

64. Pendergast, M. M.; Hoek, E. M. V., A review of water treatment membrane nanotechnologies. *Energy & Environmental Science* **2011,** *4* (6), 1946-1971.

65. Arora, G.; Sandler, S. I., Air separation by single wall carbon nanotubes: Mass transport and kinetic selectivity. *The Journal of Chemical Physics* **2006,** *124* (8), 084702.

66. Arora, G.; Sandler, S. I., Air separation by single wall carbon nanotubes: Thermodynamics and adsorptive selectivity. *The Journal of Chemical Physics* **2005,** *123* (4), 044705.

67. Ge, L.; Du, A.; Hou, M.; Rudolph, V.; Zhu, Z., Enhanced hydrogen separation by vertically-aligned carbon nanotube membranes with zeolite imidazolate frameworks as a selective layer. *RSC Advances* **2012,** *2* (31), 11793-11800.

68. Geim, A. K.; Novoselov, K. S., The rise of graphene. *Nature Materials* **2007,** *6*, 183.

69. Mermin, N. D., Crystalline Order in Two Dimensions. *Physical Review* **1968,** *176* (1), 250-254.

70. NobelPrize.org The Nobel Prize in Physics 2010. https://www.nobelprize.org/prizes/physics/2010/summary/ (accessed Thu. 9 Jul 2019).

71. Castro Neto, A. H.; Guinea, F.; Peres, N. M. R.; Novoselov, K. S.; Geim, A. K., The electronic properties of graphene. *Reviews of Modern Physics* **2009,** *81* (1), 109-162.

72. Maffucci, A.; Miano, G., Electrical Properties of Graphene for Interconnect Applications. *Applied Sciences* **2014,** *4*, 305-317.

73. Venables, J. A.; Spiller, G. D. T.; Hanbucken, M., Nucleation and growth of thin films. *Reports on Progress in Physics* **1984,** *47* (4), 399-459.

74. Meyer, J. C.; Geim, A. K.; Katsnelson, M. I.; Novoselov, K. S.; Booth, T. J.; Roth, S., The structure of suspended graphene sheets. *Nature* **2007,** *446*, 60.

75. Thompson-Flagg, R. C.; Moura, M. J. B.; Marder, M., Rippling of graphene. *EPL (Europhysics Letters)* **2009,** *85* (4), 46002.

76. Katsnelson, M. I.; Geim, A. K., Electron scattering on microscopic corrugations in graphene. *Philosophical Transactions of the Royal Society A: Mathematical, Physical and Engineering Sciences* **2008,** *366* (1863), 195-204.

77. Warner, J. H.; Schäffel, F.; Bachmatiuk, A.; Rümmeli, M. H., Chapter 3 - Properties of Graphene. In *Graphene*, Warner, J. H.; Schäffel, F.; Bachmatiuk, A.; Rümmeli, M. H., Eds. Elsevier: 2013; pp 61-127.

78. Lee, C.; Wei, X.; Kysar, J. W.; Hone, J., Measurement of the Elastic Properties and Intrinsic Strength of Monolayer Graphene. *Science* **2008,** *321* (5887), 385.

79. Zhu, Y.; Murali, S.; Cai, W.; Li, X.; Suk, J. W.; Potts, J. R.; Ruoff, R. S., Graphene and graphene oxide: synthesis, properties, and applications. *Advanced materials (Deerfield Beach, Fla.)* **2010,** *22* (35), 3906-24.

80. Balandin, A. A.; Ghosh, S.; Bao, W.; Calizo, I.; Teweldebrhan, D.; Miao, F.; Lau, C. N., Superior Thermal Conductivity of Single-Layer Graphene. *Nano Letters* **2008,** *8* (3), 902-907.

81. Bolotin, K. I.; Sikes, K. J.; Jiang, Z.; Klima, M.; Fudenberg, G.; Hone, J.; Kim, P.; Stormer, H. L., Ultrahigh electron mobility in suspended graphene. *Solid State Communications* **2008,** *146* (9), 351-355.

82. Yang, T.; Zhao, X.; He, Y.; Zhu, H., 6 - Graphene-Based Sensors. In *Graphene*, Zhu, H.; Xu, Z.; Xie, D.; Fang, Y., Eds. Academic Press: 2018; pp 157-174.

83. Bonaccorso, F.; Sun, Z.; Hasan, T.; Ferrari, A. C., Graphene Photonics and Optoelectronics. *Nature Photonics* **2010,** *4.*

84. Bunch, J. S.; Verbridge, S. S.; Alden, J. S.; van der Zande, A. M.; Parpia, J. M.; Craighead, H. G.; McEuen, P. L., Impermeable atomic membranes from graphene sheets. *Nano Letters* **2008,** *8* (8), 2458-2462.

85. Adil, S. F.; Khan, M.; Kalpana, D., 7 - Graphene-based nanomaterials for solar cells. In *Multifunctional Photocatalytic Materials for Energy*, Lin, Z.; Ye, M.; Wang, M., Eds. Woodhead Publishing: 2018; pp 127-152.

86. Bai, L.; Zhang, Y.; Tong, W.; Sun, L.; Huang, H.; An, Q.; Tian, N.; Chu, P. K., Graphene for Energy Storage and Conversion: Synthesis and Interdisciplinary Applications. *Electrochemical Energy Reviews* **2019**.

87. Leenaerts, O.; Partoens, B.; Peeters, F. M., Graphene: A perfect nanoballoon. *Applied Physics Letters* **2008,** *93* (19), 3.

88. Huang, L.; Zhang, M.; Li, C.; Shi, G., Graphene-Based Membranes for Molecular Separation. *The Journal of Physical Chemistry Letters* **2015,** *6* (14), 2806-2815.

89. Hu, S.; Lozada-Hidalgo, M.; Wang, F. C.; Mishchenko, A.; Schedin, F.; Nair, R. R.; Hill, E. W.; Boukhvalov, D. W.; Katsnelson, M. I.; Dryfe, R. A. W.; Grigorieva, I. V.; Wu, H. A.; Geim, A. K., Proton transport through one-atom-thick crystals. *Nature* **2014,** *516*, 227.

90. Cedillo, A., Quantum Mechanical Tunneling through Barriers: A Spreadsheet Approach. *Journal of Chemical Education* **2000,** *77* (4), 528.

91. Lehtinen, O.; Kotakoski, J.; Krasheninnikov, A. V.; Tolvanen, A.; Nordlund, K.; Keinonen, J., Effects of ion bombardment on a two-dimensional target: Atomistic simulations of graphene irradiation. *Physical Review B* **2010,** *81* (15), 153401.

92. Bieri, M.; Treier, M.; Cai, J.; Aït-Mansour, K.; Ruffieux, P.; Gröning, O.; Gröning, P.; Kastler, M.; Rieger, R.; Feng, X.; Müllen, K.; Fasel, R., Porous graphenes: two-dimensional polymer synthesis with atomic precision. *Chemical Communications* **2009,** (45), 6919-6921.

93. Murata, K.; Kaneko, K.; Steele, W. A.; Kokai, F.; Takahashi, K.; Kasuya, D.; Yudasaka, M.; Iijima, S., Porosity Evaluation of Intrinsic Intraparticle Nanopores of Single Wall Carbon Nanohorn. *Nano Letters* **2001,** *1* (4), 197-199.

94. Jiang, D.-e.; Cooper, V. R.; Dai, S., Porous Graphene as the Ultimate Membrane for Gas Separation. *Nano Letters* **2009,** *9* (12), 4019-4024.

95. Schrier, J., Helium Separation Using Porous Graphene Membranes. *The Journal of Physical Chemistry Letters* **2010,** *1* (15), 2284-2287.

96. Du, H.; Li, J.; Zhang, J.; Su, G.; Li, X.; Zhao, Y., Separation of Hydrogen and Nitrogen Gases with Porous Graphene Membrane. *The Journal of Physical Chemistry C* **2011,** *115* (47), 23261-23266.

97. Hauser, A. W.; Schwerdtfeger, P., Nanoporous Graphene Membranes for Efficient 3He/4He Separation. *The Journal of Physical Chemistry Letters* **2012,** *3* (2), 209-213.

98. Hauser, A. W.; Schwerdtfeger, P., Methane-selective nanoporous graphene membranes for gas purification. *Physical Chemistry Chemical Physics* **2012,** *14* (38), 13292-13298.

99. Sun, C.; Boutilier, M. S. H.; Au, H.; Poesio, P.; Bai, B.; Karnik, R.; Hadjiconstantinou, N. G., Mechanisms of Molecular Permeation through Nanoporous Graphene Membranes. *Langmuir* **2014,** *30* (2), 675-682.

100. Tao, Y.; Xue, Q.; Liu, Z.; Shan, M.; Ling, C.; Wu, T.; Li, X., Tunable Hydrogen Separation in Porous Graphene Membrane: First-Principle and Molecular Dynamic Simulation. *ACS Applied Materials & Interfaces* **2014,** *6* (11), 8048-8058.

101. Ohba, T., Consecutive Water Transport through Zero-Dimensional Graphene Gates of Single-Walled Carbon Nanohorns. *The Journal of Physical Chemistry C* **2016,** *120* (16), 8855-8862.

102. Raghavan, B.; Gupta, T., H2/CH4 Gas Separation by Variation in Pore Geometry of Nanoporous Graphene. *The Journal of Physical Chemistry C* **2017,** *121* (3), 1904-1909.

103. Suk, M. E.; Aluru, N. R., Water Transport through Ultrathin Graphene. *The Journal of Physical Chemistry Letters* **2010,** *1* (10), 1590-1594.

104. Humplik, T.; Lee, J.; O'Hern, S. C.; Fellman, B. A.; Baig, M. A.; Hassan, S. F.; Atieh, M. A.; Rahman, F.; Laoui, T.; Karnik, R.; Wang, E. N., Nanostructured materials for water desalination. *Nanotechnology* **2011,** *22* (29), 292001.

105. Cohen-Tanugi, D.; Grossman, J. C., Water Desalination across Nanoporous Graphene. *Nano Letters* **2012,** *12* (7), 3602-3608.

106. Wang, E. N.; Karnik, R., Water desalination: Graphene cleans up water. *Nat Nanotechnol* **2012,** *7* (9), 552-4.

107. Ersan, G.; Apul, O. G.; Perreault, F.; Karanfil, T., Adsorption of organic contaminants by graphene nanosheets: A review. *Water Research* **2017,** *126*, 385-398.

108. A Brief History of Quantum Mechanics. In *Quantum Mechanics: A Modern and Concise Introductory Course*, Bes, D. R., Ed. Springer Berlin Heidelberg: Berlin, Heidelberg, 2007; pp 201-214.

109. Planck, M., On the Law of Distribution of Energy in the Normal Spectrum. *Annalen der Physik* **1901,** *4*, 553.

110. Einstein, A., Concerning an Heuristic Point of View Toward the Emission and Transformation of Light. *Annalen der Physik* **1905,** *17*, 132-148.

111. Bohr, N., On the Constitution of Atoms and Molecules. *Philosophical Magazine* **1913,** *26* (6), 1-25.

112. Broglie, L. d., XXXV. A tentative theory of light quanta. *The London, Edinburgh, and Dublin Philosophical Magazine and Journal of Science* **1924,** *47* (278), 446-458.

113. Davisson, C.; Germer, L. H., Diffraction of Electrons by a Crystal of Nickel. *Physical Review* **1927,** *30* (6), 705-740.

114. Cresser, J., Quantum physics notes. *Department of Physics, Macquarie University, Australia* **2011**.

115. Heisenberg, W., Über den anschaulichen Inhalt der quantentheoretischen Kinematik und Mechanik. *Zeitschrift für Physik* **1927,** *43* (3), 172-198.

116. Dorobantu, V., The postulates of Quantum Mechanics. *arXiv preprint physics/0602145* **2006**.

117. Nottale, L.; Célérier, M.-N., Derivation of the postulates of quantum mechanics from the first principles of scale relativity. *Journal of Physics A: Mathematical and Theoretical* **2007,** *40* (48), 14471.

118. Group, T., Operator methods in quantum mecanics. University of Cambridge; pp. 18-32.

119. Leach, A. R., *Molecular modelling : principles and applications*. Prentice Hall: Harlow, England; New York, 2001.

120. Jensen, F., *Introduction to Computational Chemistry*. John Wiley \&\#38; Sons, Inc.: 2006.

121. Atkins, P.; Friedman, R., *Molecular quantum mechanics*. Oxford Univ. Press: Oxford, 2008.

122. Fermi, E., Un Metodo Statistico per la Determinazione di alcune Prioprietà dell'Atomo. *Endiconti: Accademia Nazionale dei Lincei* **1927,** *6*, 602-607.

123. Thomas, L. H., The calculation of atomic fields. *Mathematical Proceedings of the Cambridge Philosophical Society* **1927,** *23* (5), 542-548.

124. Sousa, S. F.; Fernandes, P. A.; Ramos, M. J., General Performance of Density Functionals. *The Journal of Physical Chemistry A* **2007,** *111* (42), 10439-10452.

125. Hohenberg, P.; Kohn, W., Inhomogeneous Electron Gas. *Physical Review* **1964,** *136* (3B), B864-B871.

126. Kohn, W.; Sham, L. J., Self-Consistent Equations Including Exchange and Correlation Effects. *Physical Review* **1965,** *140* (4A), A1133-A1138.

127. Dirac, P. A. M., Note on Exchange Phenomena in the Thomas Atom. *Mathematical Proceedings of the Cambridge Philosophical Society* **1930,** *26* (3), 376-385.

128.   Slater, J. C., A Simplification of the Hartree-Fock Method. *Physical Review* **1951,** *81* (3), 385-390.

129.   Becke, A. D., Correlation energy of an inhomogeneous electron gas: A coordinate-space model. *The Journal of Chemical Physics* **1988,** *88* (2), 1053-1062.

130.   Perdew, J. P., Density-functional approximation for the correlation energy of the inhomogeneous electron gas. *Physical Review B* **1986,** *33* (12), 8822-8824.

131.   Perdew, J. P., Unified theory of exchange and correlation beyond the local density approximation. In *Electronic Structure of Solids '91*, Verlag, A., Ed. Berlin, 1991; Vol. 17, pp 11-20.

132.   Lee, C.; Yang, W.; Parr, R. G., Development of the Colle-Salvetti correlation-energy formula into a functional of the electron density. *Physical Review B* **1988,** *37* (2), 785-789.

133.   Becke, A. D., Density-functional thermochemistry. IV. A new dynamical correlation functional and implications for exact-exchange mixing. *The Journal of Chemical Physics* **1996,** *104* (3), 1040-1046.

134.   Krieger, J. B.; Chen, J.; Iafrate, G. J.; Savin, A., Construction of An Accurate Self-interaction-corrected Correlation Energy Functional Based on An Electron Gas with A Gap. In *Electron Correlations and Materials Properties*, Gonis, A.; Kioussis, N.; Ciftan, M., Eds. Springer US: Boston, MA, 1999; pp 463-477.

135.   Tao, J.; Perdew, J. P.; Staroverov, V. N.; Scuseria, G. E., Climbing the Density Functional Ladder: Nonempirical Meta--Generalized Gradient Approximation Designed for Molecules and Solids. *Physical Review Letters* **2003,** *91* (14), 146401.

136.   Van Voorhis, T.; Scuseria, G. E., A novel form for the exchange-correlation energy functional. *The Journal of Chemical Physics* **1998,** *109* (2), 400-410.

137.   Becke, A. D., Density-functional thermochemistry. III. The role of exact exchange. *The Journal of Chemical Physics* **1993,** *98* (7), 5648-5652.

138.   Tirado-Rives, J.; Jorgensen, W. L., Performance of B3LYP Density Functional Methods for a Large Set of Organic Molecules. *Journal of Chemical Theory and Computation* **2008,** *4* (2), 297-306.

139.   Walker, M.; Harvey, A. J. A.; Sen, A.; Dessent, C. E. H., Performance of M06, M06-2X, and M06-HF Density Functionals for Conformationally Flexible Anionic Clusters: M06 Functionals Perform Better than B3LYP for a Model System with Dispersion and Ionic Hydrogen-Bonding Interactions. *The Journal of Physical Chemistry A* **2013,** *117* (47), 12590-12600.

140.   Zhao, Y.; Truhlar, D. G., The M06 suite of density functionals for main group thermochemistry, thermochemical kinetics, noncovalent interactions, excited states, and transition elements: two new functionals and systematic testing of four M06-class functionals and 12 other functionals. *Theoretical Chemistry Accounts* **2008,** *120* (1), 215-241.

141.   Zhao, Y.; Schultz, N. E.; Truhlar, D. G., Exchange-correlation functional with broad accuracy for metallic and nonmetallic compounds, kinetics, and noncovalent interactions. *J Chem Phys* **2005,** *123* (16), 161103.

142.   Perdew, J. P.; Burke, K.; Ernzerhof, M., Generalized Gradient Approximation Made Simple. *Physical Review Letters* **1996,** *77* (18), 3865-3868.

143.   Schmider, H. L.; Becke, A. D., Density functionals from the extended G2 test set: Second-order gradient corrections. *The Journal of Chemical Physics* **1998,** *109* (19), 8188-8199.

144.   Amovilli, C.; Barone, V.; Cammi, R.; Cancès, E.; Cossi, M.; Mennucci, B.; Pomelli, C. S.; Tomasi, J., Recent Advances in the Description of Solvent Effects with the Polarizable Continuum Model. In *Advances in Quantum Chemistry*, Löwdin, P.-O., Ed. Academic Press: 1998; Vol. 32, pp 227-261.

145.   Dennington, R.; Keith, T. A.; Millam, J. M. *GaussView Version 5.0.8*, 2016.

146.   Lindahl, E.; Edholm, O., Mesoscopic Undulations and Thickness Fluctuations in Lipid Bilayers from Molecular Dynamics Simulations. *Biophysical Journal* **2000,** *79* (1), 426-433.

147.   Bochicchio, D.; Monticelli, L., Chapter Five - The Membrane Bending Modulus in Experiments and Simulations: A Puzzling Picture. In *Advances in Biomembranes and Lipid Self-Assembly*, Iglič, A.; Kulkarni, C. V.; Rappolt, M., Eds. Academic Press: 2016; Vol. 23, pp 117-143.

148.   Tavares, I. S.; Figueiredo, C. F. B. R.; Magalhães, A. L., The Inner Cavity of a Carbon Nanotube as a Chemical Reactor: Effect of Geometry on the Catalysis of a Menshutkin SN2 Reaction. *The Journal of Physical Chemistry C* **2017,** *121* (4), 2165-2172.

149.   Smith, A. R.; Klosek, J., A review of air separation technologies and their integration with energy conversion processes. *Fuel Processing Technology* **2001,** *70* (2), 115-134.

150.   Breck, D. W., *Zeolite molecular sieves: structure, chemistry, and use*. Wiley: 1973.

151.   Sing, K. S. W.; Williams, R. T., The Use of Molecular Probes for the Characterization of Nanoporous Adsorbents. *Particle & Particle Systems Characterization* **2004,** *21* (2), 71-79.

152.   Webster, C. E.; Drago, R. S.; Zerner, M. C., A Method for Characterizing Effective Pore Sizes of Catalysts. *The Journal of Physical Chemistry B* **1999,** *103* (8), 1242-1249.

153.   Webster, C. E.; Cottone, A.; Drago, R. S., Multiple Equilibrium Analysis Description of Adsorption on Na−Mordenite and H−Mordenite. *Journal of the American Chemical Society* **1999,** *121* (51), 12127-12139.

154.   Tang, S.; Cao, Z., Adsorption of nitrogen oxides on graphene and graphene oxides: Insights from density functional calculations. *The Journal of Chemical Physics* **2011,** *134* (4), 044710.

155.   Humphrey, W.; Dalke, A.; Schulten, K., VMD: Visual molecular dynamics. *Journal of Molecular Graphics* **1996,** *14* (1), 33-38.

156.   Kong, L.; Enders, A.; Rahman, T.; Dowben, P., Molecular adsorption on graphene. *Journal of Physics: Condensed Matter* **2014,** *26*, 443001.

157.   Lazar, P.; Karlický, F.; Jurečka, P.; Kocman, M.; Otyepková, E.; Šafářová, K.; Otyepka, M., Adsorption of Small Organic Molecules on Graphene. *Journal of the American Chemical Society* **2013,** *135* (16), 6372-6377.